12-2018

Intrinsic Geometrical Constraints of Spontaneously Excited Leidenfrost Drops

Jesse Edward Bergen
Clemson University, jeberge@g.clemson.edu

Intrinsic geometrical constraints of spontaneously excited Leidenfrost drops

---

A Thesis
Presented to
the Graduate School of
Clemson University

In Partial Fulfillment
of the Requirements for the Degree
Master of Science
Mechanical Engineering

---

by
Jesse Edward Bergen
December 2018

Accepted by:
Dr. Joshua Bostwick, Committee Chair
Dr. John Saylor
Dr. Daniel Fant

Abstract

A liquid drop placed on a heated surface above the Leidenfrost temperature will levitate on a vapor cushion. The static shape of these non-wetting Leidenfrost drops is that of a flattened sphere, reflecting the balance between gravitational, surface tension and lubrication pressures. In this thesis, we study Leidenfrost drops on curved substrates where we observe spontaneous star-shaped surface oscillations of characteristic frequency and mode number. Experiments are conducted using six different liquids and the temporal response of the observed modes $n = 2 - 13$ is analyzed to define the oscillation spectrum. We observe that large drops oscillate with a constant frequency, while small drop frequencies are strongly dependent upon liquid volume. A simple mathematical model is developed using a hydrodynamic stability analysis and shows reasonable agreement with our large experimental data set. Scaling arguments are used to collapse the data which allows generalized statements to be made regarding the physics governing star oscillations. In addition, we observe more complex dynamics such as mode doubling where two distinct modes are simultaneously excited at different frequencies and modal dominance where one mode persists over large ranges of parameter space previously thought to be occupied by another mode. Lastly, we conclude by offering some qualitative observations of Leidenfrost shape instabilities in other complex substrate geometries.

Table of Contents

List of Tables

List of Figures

Chapter 1

Introduction

1.1 Surface tension driven phenomena

A liquid drop will oscillate about its equilibrium shape reflecting a balance between the inertia of the fluid and the restoring force of surface tension. Rayleigh (1879) used a linear stability analysis to show a spherical drop with oscillate with characteristic frequency

$$f = \frac{1}{2\pi}\sqrt{\frac{\sigma n(n-1)(n+2)}{\rho R^3}} \tag{1.1}$$

where n represents the oscillation mode number, ρ is liquid density, σ is surface tension and R is the equilibrium drop radius. Trinh et al. (1982) verified these results experimentally by observing the $n = 2-4$ modes of oscillation in liquid drops immersed in a secondary liquid. Figure 1.1 shows these polygonal shapes appearing during drop oscillation for $n = 2-4$. In this thesis, we use the Leidenfrost effect to levitate drops where we observe modes of oscillation ranging from $n = 2-13$ and give interpretations on the mechanisms of mode selection.

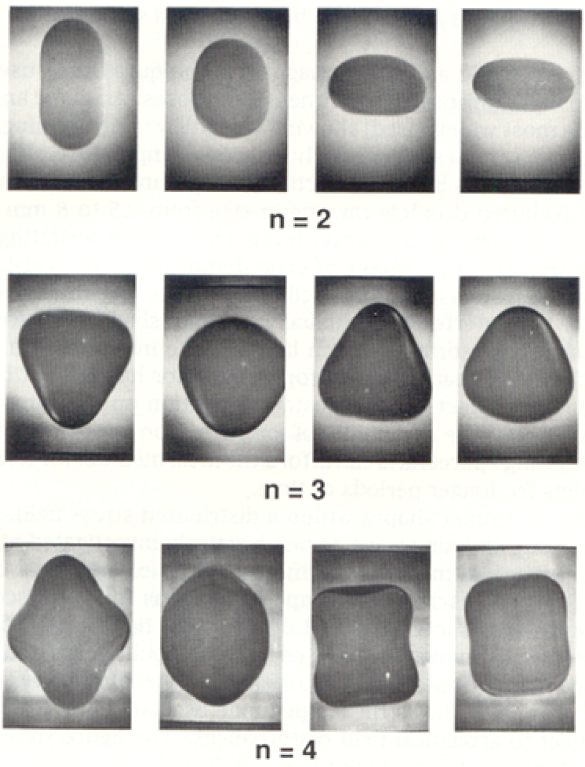

Figure 1.1: Experimental image from Trinh et al. (1982) showing oscillations of a liquid drop immersed in a secondary fluid.

Capillary oscillations have been studied extensively in the literature. In experiments, liquid drops are typically forced to oscillate by interaction with their surroundings. One common method to induce drop oscillations is through mechanical excitation. Drops which strongly adhere to the vibrating substrate in a wetting situation are known to oscillate harmonically at the prescribed forcing frequency (Okada and Okada, 2006). In contrast, weakly pinned or non-wetting drops can exhibit parametric resonance (Yoshiyasu et al., 1996; Brunet and Snoeijer, 2011). It becomes obvious that contact between liquid drops and their surroundings affect the dynamics of drop oscillations leading to recent studies on the effect of liquid contact with a solid support during drop oscillation (Bostwick and Steen, 2009; Prosperetti, 2012; Chang et al., 2013; Bostwick and Steen, 2013a,b, 2015). To remove boundary effects in practice, it is necessary to develop techniques to prevent liquid-solid contact.

1.2 Non-wetting phenomena

Liquid solid contact is known to attenuate drop oscillation dynamics such as in sessile drop experiments (Vukasinovic et al., 2007) or a liquid drop immersed in a secondary liquid bath (Trinh and Wang, 1982). Several scenarios exist in which a liquid drop can be virtually isolated from its surroundings. Examples include microgravity (Wang et al., 1996), immersion in a secondary liquid bath (neutral buoyancy) (Trinh et al., 1982), acoustic levitation (Trinh et al., 1996; Shen et al., 2010), electromagnetic levitation (Trinh et al., 1996; Fautrelle et al., 2005) and support by uniform airflow from underneath (Nelson and Gokhale, 1972; Perez et al., 1999; Hervieu et al., 2001; Jones and Saylor, 2009; Snoeijer et al., 2009; Brunet and Snoeijer, 2011; Bouwhuis et al., 2013). One isolation technique which has been the focus of several recent studies uses the Leidenfrost phenomenon in order to prevent liquid-solid contact (Snezhko

et al., 2008; Ma et al., 2017; Ma and Burton, 2018). This technique inherently excites drop oscillations as will be discussed in section 1.3. The non-wetting condition is realized experimentally using the Leidenfrost phenomenon to levitate the drop on its own vapor cushion to provide a free surface on which to investigate the spontaneous axisymmetric large amplitude oscillations of liquid drops.

1.3 Leidenfrost phenomena

Liquid drops placed on a surface heated sufficiently above the liquid saturation temperature are subjected to rapid vaporization. Above a critical surface temperature, these drops are supported on a layer of their own vapor due to the pressure the vapor layer exerts on the bottom drop surface. The vapor pressure is sufficient to balance the weight of the drop and keeps the drop from contacting the heated surface. These drops persist for several minutes before complete vaporization. This phenomenon may be recognized in a more familiar context as film boiling of relatively small volumes of liquid (cf. Figure 1.2) and was first documented by German medical doctor J. G. Leidenfrost in 1756 (Leidenfrost, 1756). We use the Leidenfrost phenomenon to levitate a liquid drop in order to create a non-contacting liquid-vapor interface.

The surface temperature T_s associated with the onset of stable film boiling is called the Leidenfrost temperature T_L and is depicted in Figure 1.2. The onset of stable film boiling and thus T_L is characterized by a minimum wall heat flux q''_{min}, which is caused by the complete formation of the thermally insulating vapor layer whose thermal conductivity is several orders of magnitude lower than the liquid phase. For T_s ranging from T_L to moderately above T_L, the primary mechanism of heat transfer is conduction through the vapor layer (Gottfried et al., 1966; Avedisian

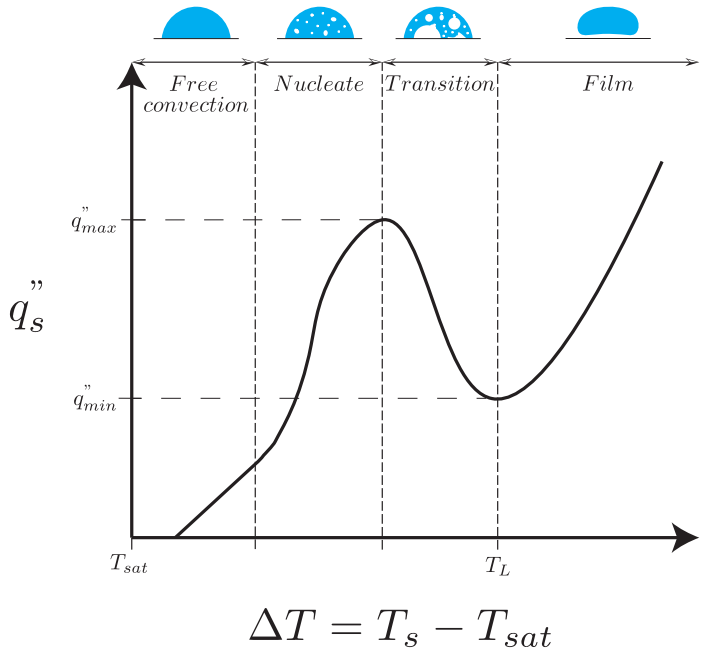

Figure 1.2: Boiling curve labelled with figures depicting the associated boiling regimes. T_L is located at the point of minimum heat flux q''_s.

and Koplik, 1987). As T_s increases above T_L, q''_s increases due to increased conduction through the vapor layer caused by the larger temperature difference leading to a reduction in vaporization time τ. For $T_s > T_L$, the increase in q''_s is shown in Figure 1.2 and the commensurate reduction in τ in Figure 1.3.

T_L may be determined experimentally by depositing a single drop on a surface heated to the liquid saturation temperature and observing the time required for total vaporization τ. Incrementally increasing surface temperature and repeating the process for a large range of temperatures above the liquid saturation temperature yields Figure 1.3 which plots τ against T_s. In order to accurately determine T_L, drops must be of equal volume and the surface should be polished between each measurement (Baumeister et al., 1970; Baumeister and Simon, 1973; Peterson and Zaalouk, 1971; Bernardin and Mudawar, 1999). In addition, care must be taken to avoid splash-

ing and unwanted drop deformation which may lead to decreased vaporization times owing to either droplet ejection during splashing or due to the larger near contact area of a deformed liquid drop. The surface temperature at which τ is maximized is the identified as T_L. Above this temperature, the liquid drop is suspended above the heated surface on a film of its own vapor. Figure 1.3 shows the vaporization time of a $.04mL$ volume isopropanol drop on aluminum and brass substrates with respect to surface temperature. For this drop T_L is roughly determined to be $155°C$ on brass and $170°C$ on aluminum.

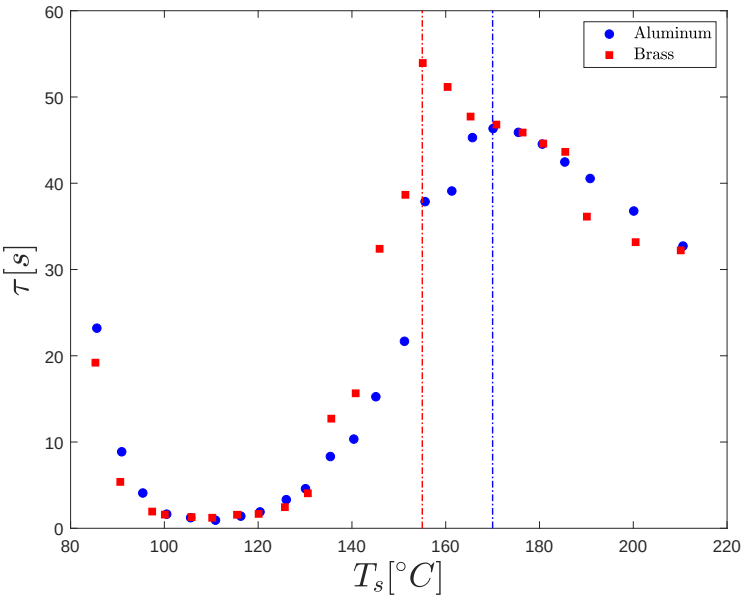

Figure 1.3: Lifetime τ of an isopropanol droplet of volume $V = .04mL$, as a function of the surface temperature T_s on alumium and brass substrates.

T_L may be higher for non-isothermal substrates (Baumeister et al., 1970). Here the brass substrate may be considered relatively more isothermal than the aluminum substrate due to its higher combined thermal properties density ρ, specific heat c and thermal conductivity k. This is speculated to be the reason T_L is slightly higher for

the aluminum substrate.

1.4 Leidenfrost drops

Drops experiencing complete film boiling with no contact to the substrate are considered to be in the Leidenfrost state and are termed Leidenfrost drops. In this thesis we focus on spontaneous azimuthal surface shape oscillations of Leidenfrost drops which we will refer to as Leidenfrost star oscillations. Figure 1.4 shows a typical $n = 5$ Leidenfrost star oscillation of a water drop exhibiting well defined lobes around the drop circumference.

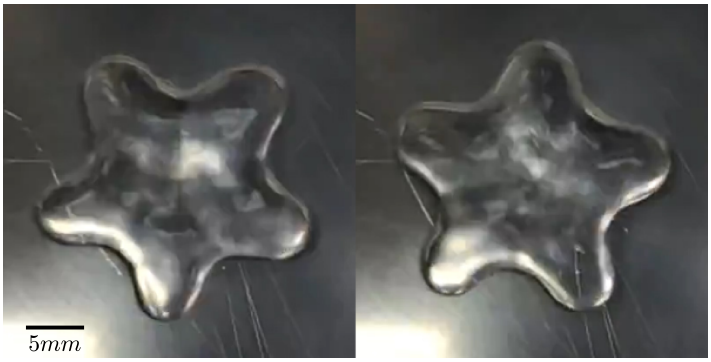

Figure 1.4: Typical water drop oscillating as $n = 5$ mode. Frames are taken during two extrema one half period apart.

Leidenfrost drops are unique to the situations discussed previously because these drops are highly mobile and free to move under any external force. Due to their high mobility experimental studies typically use a curved substrate to confine liquid drops in a shallow bowl in order to study both the static equilibrium shape and star oscillations. Several recent studies characterize the static equilibrium shape

of Leidenfrost drops which will be discussed in section 1.4.1 (Biance et al., 2003; Burton et al., 2012; Quéré, 2013; Caswell, 2014). The interaction between the liquid interface of oscillating Leidenfrost drops and their surroundings is generally limited to the underlying vapor layer. The dynamic geometry of the vapor layer is speculated to influence Leidenfrost star oscillations which will be discussed in section 2.6.4 (Burton et al., 2012; Caswell, 2014; Ma et al., 2017; Ma and Burton, 2018).

1.4.1 Equilibrium drop shape

The equilibrium shape of Leidenfrost drops depends on the balance of surface tension and gravity, thus drop size directly influences drop shape. The capillary length l_c is used to characterize drop size with

$$l_c = \sqrt{\frac{\sigma}{\rho g}} \tag{1.2}$$

where σ is the liquid surface tension, ρ is the liquid density and g is gravitational acceleration. l_c is essentially a measure of surface tension effects to gravitational effects.

For small drops, with radius $R < l_c$, shape is dominated by surface tension causing these drops to take the shape of spheres with a slightly flattened bottom closest to the heated surface. Here large Laplace pressures dominate gravitational effects. These drops were never observed to exhibit Leidenfrost star oscillations and thus are omitted from this study. The smallest drops exhibiting star oscillations are observed to have a radius just above the liquid's capillary length $R/l_c \approx 1$.

Large drops $R > l_c$ are the focus of this study. These drops are more significantly influenced by gravity and tend to flatten to the shape shown in Figure 1.5. Recent studies have determined these drops to have a thickness of roughly $2l_c$ (Biance

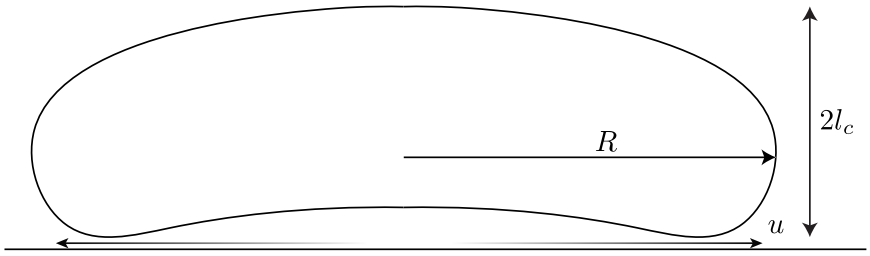

Figure 1.5: Illustration of a large liquid drop $R > l_c$

et al., 2003; Quéré, 2013). Biance et al. (2003) finds the vaporization of large drops $R > l_c$ occurs primarily at the bottom interface into the vapor layer. Avedisian and Koplik (1987) finds that the drop weight causes a radial Poiseuille outward flow of vapor from the center of the drop. Thus, the vapor flux leaving the bottom interface of large drops results in the radial outflow of vapor u (cf. Figure 1.5). The thickness of the vapor layor has been determined experimentally (Biance et al., 2003; Burton et al., 2012; Caswell, 2014) to be on the order of 10 µm to 100 µm. Thus, thin film lubrication approximation has been applied to describe the vapor flow theorectically (Biance et al., 2003; Pomeau et al., 2012; Quéré, 2013).

1.4.2 Drop dynamics

Large Leidenfrost drops are subjected to complex dynamical motion initiated by the constant surface temperature T_s imposed by the substrate and the subsequent rapid evaporative vapor flow u. These drops are reported to sponatenously translate (Bouillant et al., 2018) and rotate (Holter and Glasscock, 1952). In addition, several hydrodynamic instabilities are reported. One instability, a Rayleigh-Taylor type instability, is inherent due to buoyancy forces imposed by the underlying vapor. Burton et al. (2012) uses laser-light interference to image the bottom interface of Leidenfrost drops and finds the vapor layer forms a concave pocket of vapor pressing into the liq-

uid interface. Following a first order perturbation analysis Biance et al. (2003) finds a critical radius of Leidenfrost drops on a flat plate to be $R_c = 3.84l_c$ in which a drop of radius exceeding this critical radius will experience vapor bubbles rising from this vapor pocket and forcibly breaking through the upper liquid surface. Experimentally, Biance et al. (2003) observed a critical radius of roughly $R_{max} = 4l_c$, beyond this limit, vapor bubbles appear on flat plates. This instability has also been reported in drops supported by uniform airflow from underneath (Snoeijer et al., 2009) who finds that the maximum radius of these drops to be roughly $R_{max} > 4l_c$ in agreement with Biance et al. (2003). Snoeijer et al. (2009) and Perrard et al. (2012) mention that a curved substrate improves the stability of large drops. We use a curved substrate in our experiments in order to suppress this instability as will be discussed in section 2.2.

Tokugawa and Takaki (1994); Shahriari et al. (2018) have studied thermal instabilites such as Marangoni convection which may play a role in Leidenfrost drop dynamics due to the temperature gradient presence at the top and bottom surfaces. Additional hydrodynamic instabilities have been reported including oscillations of the equilibrium radius R (Brunet and Snoeijer, 2011; Caswell, 2014), oscillations of the vertical center of mass (Brunet and Snoeijer, 2011; Caswell, 2014) and oscillatons of the azimuthal surface shape termed here as star oscillations. (Holter and Glasscock, 1952; Wachters et al., 1966; Baumeister et al., 1977; Adachi and Takaki, 1984; Takaki and Adachi, 1985; Tokugawa and Takaki, 1994; Strier et al., 2000; Snezhko et al., 2008; Ma et al., 2017; Ma and Burton, 2018). Using an idealized surface curvature, Ma et al. (2017) reports azimuthal surface shape oscillations for drops sizes up to $R = 9l_c$. These larger drops exhibited mode numbers higher than typically reported for this type of oscillation. Using a curved surface similiar to Ma et al. (2017) we observe Leidenfrost star oscillations for drops up to $R = 9l_c$ and for mode numbers

$n = 2 - 13$.

1.4.3 Motivation

Illuminating the physics governing Leidenfrost star oscillations may be extended to other situations in which geometrical patterns emerge on liquid surfaces better known as pattern formation. Leidenfrost star oscillations are still not well understood as is made apparent in a recent publication by Brunet (2018) who reviews the current state of research regarding spontaneous Leidenfrost star oscillations and highlights the current disagreement on whether oscillation frequency depends on drop radius. This disagreement brings to light the lack of understanding of the physics governing this phenomenon allowing this fundamental study to clarify the dependence of parameters such as drop radius on the frequency spectrum further illuminating the governing physics. A clear fundamental understanding of the physics at play in these drops and vapor layer may play a role in nuclear reactor cooling systems. The stability and control of the vapor layer is paramount in nuclear reactors as the complete formation of the vapor layer allows a dangerous increase in surface temperature in cooling channels potentially leading to catastrophic failure (Bergles et al., 1981). Understanding the physics governing Leidenfrost star oscillatons may provide insight into the stability of this vapor layer. Another direct application of Leidenfrost star oscillations is given by Hervieu et al. (2001) and Haumesser et al. (2002) who propose that large amplitude oscillations may be exploited to determine properties of highly dangerous liquids.

Chapter 2

Leidenfrost star oscillations

This chapter opens with a brief literature review on the theorectical and experimental background of preceding Leidenfrost star oscillation studies. This sets the stage for our fundamental investigation of this phenomenon which is still not well understood. A simplified mathematical model is derived in order to compare our experimental results to the well known theory of capillary oscillations pioneered by Rayleigh (1879). We describe the experimental setup and the method used to generate our large dataset. Results are then presented in their raw form. Our discussion of these results starts by introducing scaling factors in order to present the experimental data in such a way that definitive statements may be made for any oscillating Leidenfrost drop for every liquid used in this study. These scaling factors allow us to furthur elucidate the underlying physics governing the spontaneous star-shape oscillations of Leidenfrost drops. Finally, several characteristics of oscillating Leidenfrost drops are reported.

The azimuthal surface shape of Leidenfrost drops is observed to spontaneously oscillate with characteristic frequency and shape. These oscillations are referred to here as star oscillations as they take on the form of a star with a discrete number of

outer lobes protruding outward along the drop circumference. The number of lobes corresponds to the mode number n. Figure 1.4 shows a typical $n = 5$ oscillating water drop at an extrema showing well defined lobes around the drop circumference. Holter and Glasscock (1952) were the first to report on these star oscillations in the Leidenfrost state. Since then, this phenomenon has been the focus of several studies (Wachters et al., 1966; Baumeister et al., 1977; Adachi and Takaki, 1984; Takaki and Adachi, 1985; Tokugawa and Takaki, 1994; Strier et al., 2000; Snezhko et al., 2008; Ma et al., 2017; Ma and Burton, 2018).

2.1 Leidenfrost star oscillation background

The origin of the star oscillations is still not well understood. Some proposed mechanisms behind these oscillations include: liquid-solid contact, Marangoni convection and viscous shear stress generated at the liquid-vapor interface. Liquid-solid contact during star oscillations has been ruled out by Holter and Glasscock (1952) using an electrical circuit connected to the liquid and solid substrate. Tokugawa and Takaki (1994) propose these oscillations are caused by modulations of surface tension at the periphery of Leidenfrost drops due to periodic contact with hot vapor and cooler air during oscillation. Temperature difference between the bottom liquid-vapor interface and the top liquid-vapor interface is speculated to generate a Marangoni convection flow in the liquid due to a gradient in surface tension (Baumeister et al., 1977; Adachi and Takaki, 1984; Tokugawa and Takaki, 1994; Quéré, 2013). This theory is supported by experimental observations of internal convective flows by Snezhko et al. (2008) and further supported by a linear stability analysis by Tokugawa and Takaki (1994) who predict periodic temporal fluctuations in the drop radius. These temporal flucuations would provide the expected condition for parametric forcing (Ma and

Burton, 2018). However, similar oscillations have been reported in drops suspended by uniform air flow from underneath a porous surface suggesting thermal effects are not significant in the formation of these sustained oscillations (Nelson and Gokhale, 1972; Perez et al., 1999; Hervieu et al., 2001; Brunet and Snoeijer, 2011; Bouwhuis et al., 2013).

Takaki and Adachi (1985) develop a hydrodynamical model for a flattened drop by applying shallow water theory and deriving a set of governing equations for Leidenfrost star oscillations. They consider small amplitude oscillations and find a solution in terms of normal modes and find good agreement with experiment. Ma et al. (2017) adopts the same model to describe Leidenfrost star oscillations. In section 2.4, we develop a simplified 2-dimensional model for flattened Leidenfrost drops which we will then use to discuss agreement between our model and our experimental values.

2.2 Experiment

2.2.1 Experimental setup

The amount of liquid levitating on planar substrates is limited by the formation of vapor bubbles beneath the liquid which can no longer escape at the edges and rises through the liquid (Biance et al., 2003). Stable levitation is only possible for relatively small drops on flat plates. Suitable geometry can prevent the formation of vapor bubbles which tend to expand upwards into the liquid causing this inverse Rayleigh-Taylor instability resulting in rising vapor bubbles. Larger volumes of liquid can be levitated provided the evaporating vapor can easily escape from underneath the drop. This is accomplished by using a curved substrate where the vapor has a path everywhere to easily escape. A curved substrate can provide an accessible

path for the vapor to escape from beneath the liquid without the formation of vapor chimneys (Perrard et al., 2012).

Experiments were run using several 360 brass and 6061 aluminum substrates of various surface geometries. Each substrate is machined in a concave manner resembling a shallow bowl, confining the liquid to the center for imaging. The top surface profile of each substrate is idealized for suppressing the inverse Rayleigh-Taylor instability mentioned previously for each liquid. The radius of curvature of these plates is choosen to satisfy the condition $l_c/R = .03$ as discussed in Ma et al. (2017). The substrate is placed on top of a hotplate surface and the hotplate-substrate system is leveled using a DXL3605 Dual Axis Digital Angle Protractor with a resolution of 0.01° and were leveled to within $.1^\circ$ in each direction for experiments. A Thermo-Scientific Super-Nuova hotplate is used to control heating of the substrates up to temperatures of 723 K. A K-type (Ni Cr + and Ni Al -) thermocouple is inserted into a 0.0625 in diameter hole machined to a depth of 0.25 in into the side of each substrate in order to monitor bulk substrate temperature. Substrate temperature is displayed on a FLIR TG56 infrared thermometer. Liquids are heated to their respective boiling temperatures before deposition onto the heated surface. From this, liquid temperatures during the Leidenfrost state are assumed to be just below the boiling temperature as found by Boutigny (1843). B+D syringes are used to deposit liquid onto the substrate top surface. A 12 megapixel camera recorded all experiments at a frame rate of 240 Hz from directly above the experimental setup as depicted in Figure 2.1.

Experiments are performed using six liquids: distilled water, acetone, isopropyl alcohol, methanol, ethanol (denatured) and liquid nitrogen. In experiments run with liquid nitrogen, the substrate did not require heating due to its relatively low Leidenfrost temperature. Relevant liquid properties at each liquid's boiling temperature are

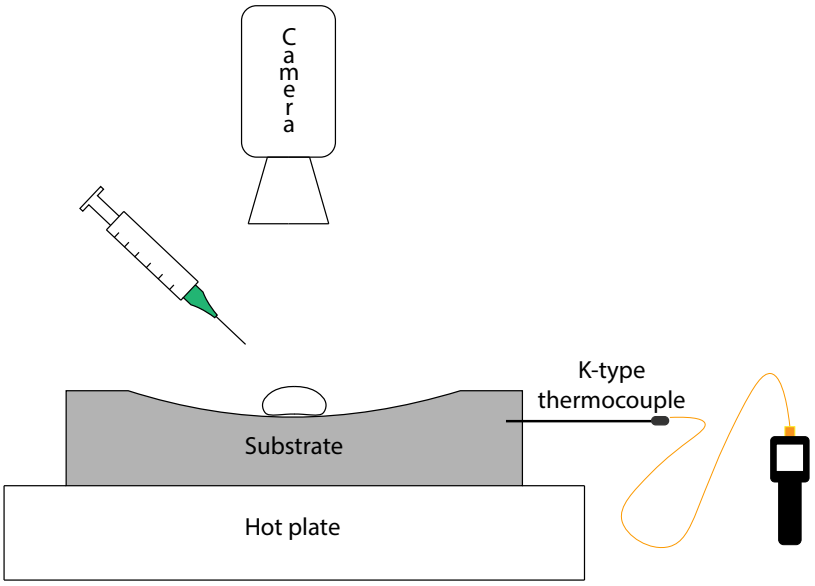

Figure 2.1: Schematic of the experimental setup.

given in Table 2.1. Liquid properties of concern here are liquid density ρ in kg/m^3, liquid viscosity η in mPa $\cdot$ s, interfacial surface tension σ in mN/m, capillary length l_c in mm and boiling temperature T_B in K. Values for all liquid properties are taken from Lemmon et al. (2011).

Surface tension σ and density ρ both appear in the mathematical model for oscillation frequency equation 2.10 and are therefore of utmost importance in describing this phenomenon. The significance of surface tension here is that it acts as the restoring force during oscillations, as it always acts to minimize surface area in an effort to attain the static circular equilibrium drop shape as discussed previously.

2.2.2 Experimental method

Substrates are heated beyond each liquid's corresponding Leidenfrost temperature in order to induce the Leidenfrost state. Each liquid is deposited via syringe

Liquid	ρ	η	σ	l_c	T_B
Water	958	0.282	59.0	2.5	373
Acetone	727	0.242	18.2	1.6	329
Isopropanol	723	0.460	15.7	1.5	356
Methanol	748	0.295	18.9	1.6	338
Ethanol	750	0.420	18.6	1.6	352
Liquid Nitrogen	807	0.162	8.90	1.1	77

Table 2.1: Liquid properties at their respective boiling temperatures. Density ρ in kg/m^3, viscosity η in mPa $\cdot$ s, surface tension σ in mN/m, capillary length l_c in mm and boiling temperature T_B in K.

onto the substrate top surface. Videos are recorded from above as the liquid evaporates. During this time, drops are observed to undergo the star oscillation instability. This instability appears along the periphery of the liquid drop in the form of azimuthal oscillations giving the drop the appearance of a star with varying numbers of outer lobes as seen in Figure 1.4. Videos are analyzed frame-by-frame using Adobe Premiere Pro CC software and processed using the NIH ImageJ software application in order to obtain the frequency of oscillations f, radius R and mode number n for each oscillating drop. Bulk substrate temperature, along with the known substrate geometry and material are also recorded. Drop radius R was extracted by overlaying two frames of a drop exhibiting star oscillations at an extrema and one half period later. Frames were exported from a 240 fps video using the method depicted in Figure 2.2 where the known length scale is taken as the substrate diameter d. From this known length, the radius of each drop is determined using ImageJ to measure the diameter of the drop at each local maximum and local minimum as shown in Figure 2.2. These measurements are averaged and divided by two giving the characteristic radius of each drop. The reason for using this method is due to the fact that these drops are not always uniformly circular as in the case of mode doubling which will be discussed in Section 2.6.2.

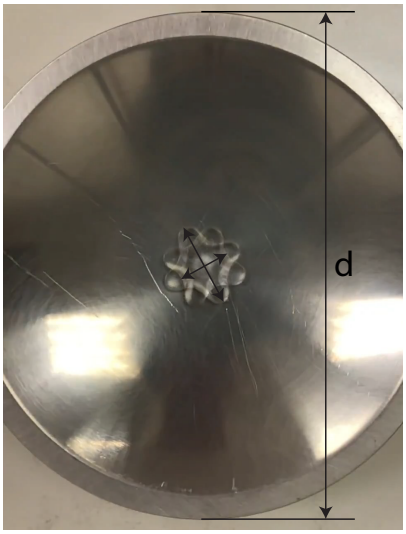

Figure 2.2: Two frames overlaid a half period apart exported from a video of a $n = 4$ water drop to illustrate the method of extracting experimental data.

The oscillation frequency f of each drop is determined by counting the number of frames in Adobe Premiere Pro for one full period of oscillation. This is performed three times for each drop to generate an average frequency value. Drops of high frequency are reported; however, it should be noted that the limited camera frame rate caused a higher degree of uncertainty in f measurements. The mode number n of each drop is found by counting the number of lobes appearing along the drop circumference during oscillation.

2.3 Experimental results

This section presents the experimental results obtained from the previously described experimental method. Results are presented in terms of oscillation frequency f in Hertz, drop radius R in meters, mode number n, and liquid. The raw data is presented for i) fixed liquid and ii) fixed mode number n. Scaling factors are then

introduced to collapse the data in an effort to elucidate the physics governing these oscillations. All error bars presented here correspond to 95% confidence intervals. A discussion of several interesting observations of oscillating Leidenfrost drops is provided. Lastly, the mechanics of star oscillations are discussed relating literature to experimental observations.

2.3.1 Unscaled data

A total of 360 independent experimental observations of Leidenfrost star oscillations are presented, generating a significant data set for all six liquids. This large data set allows for a high degree of confidence in the measured experimental values as indicated by relatively small confidence intervals for most values. A summary of the number of observed modes for each liquid is provided in Table 2.2. Leidenfrost star oscillations are observed for frequencies ranging from $f = 3\text{Hz} - 84\text{Hz}$, radii ranging from $R = 2\text{mm} - 23\text{mm}$ and modes ranging from $n = 2 - 13$. We define organized, uniform, self-reinforced oscillations as fully developed oscillations with clear, uniform extrema appearing every half period. Data is only reported for fully developed oscillations. Otherwise stated transient motion is not our concern.

Figure 2.3 shows modes $n = 2 - 13$ observed for a water drop. Figure A.1 showing all observed modes for each liquid is provided in Appendix A. The relative size of each drop is preserved, allowing direct size comparison between different mode numbers for typical oscillating water drops. As shown in Figure 2.4, f generally decreases with increasing R. It should be noted that these are the general size and shape of typical oscillating water drops; however, fully developed oscillating drops of atypical size and shape were also observed. These drops will be discussed and compared to typical star oscillations later.

Figure 2.3: All observed modes $n = 2 - 13$ for a water drop.

n	**Water**	**Acetone**	**Isopropanol**	**Methanol**	**Ethanol**	**Liquid Nitrogen**
2	6	3	11	7	6	5
3	5	7	3	3	7	12
4	11	4	4	4	3	4
5	14	5	1	3	1	10
6	18	6	1	4	2	7
7	7	9	3	3	4	8
8	7	8	6	14	5	3
9	3	7	12	7	5	9
10	7	2	9	10	5	0
11	5	1	4	6	4	0
12	4	0	1	1	1	0
13	3	0	0	0	0	0

Table 2.2: Number of each mode n observed for all six liquids

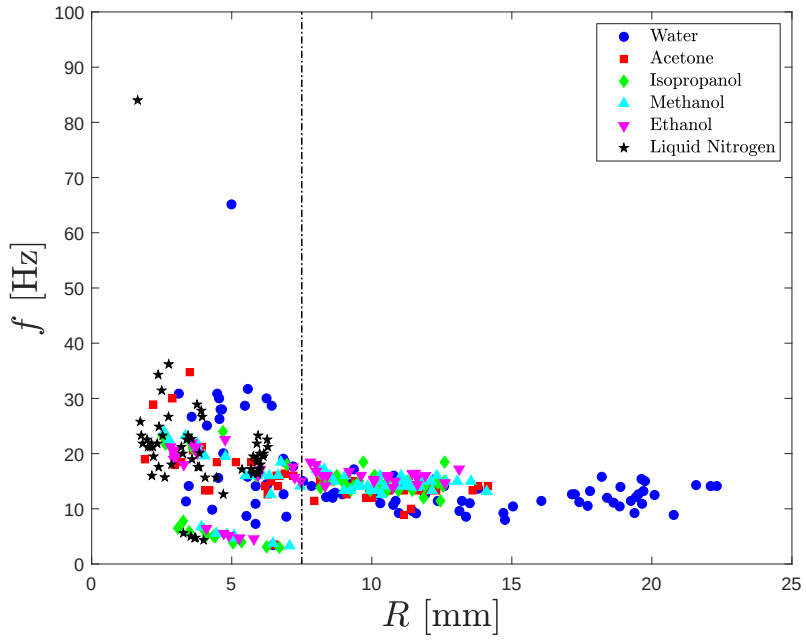

Figure 2.4: Oscillation frequency f against radius R for each liquid.

Figure 2.4 presents the measured drop oscillation frequency f in Hertz with respect to the measured radius R in meters during fully developed oscillations for the six liquids. The largest drops displaying fully developed star oscillations were observed for water with radii up to 23 mm as shown by the blue markers to the far right in Figure 2.4. The smallest of these drop oscillations were observed for liquid nitrogen down to $R = 1.6$mm. Generally water drops were observed to be larger than the other liquids. Similarily liquid nitrogen drops were observed to be smaller than the other liquids. Drops of acetone, isopropanol, methanol and ethanol were all observed to be roughly the same size. This can clearly be seen in Figure 2.4 where water drops are observed over a large range of R while drops of liquid nitrogen are observed over a small range of R, limited to smaller values of R. Later, a scaling will be introduced to collapse this data in R in order to make definitive statements about these oscillations for all liquids used in this study.

One striking feature of Figure 2.4 is the appearance of a nearly constant f for all drops of $R > 7$mm. The frequency f of smaller drops is shown to vary non-monotonically in R. However, by following a single $n = 5$ water drop over several minutes we see that reduction in radius R through vaporization results in an increase in frequency f (cf. Figure 2.5). Although this drop is larger than the 7 mm threshold, we see a larger dependence of f on R as the drop reduces in radius. We find this dependence to be true for all oscillating Leidenfrost drops of fixed mode number n. Oscillating drops of liquid nitrogen were only observed for $R < 6$mm; however f still appears to become increasingly independent of drop size for larger R. The results in their raw form do not allow generalized statements to be made regarding f dependence on R for all liquids. Therefore, we can not say all liquid drops of $R > 7$mm oscillate at a constant f. In section 2.5, we introduce a scaling in R to quantify drop sizes independent of the liquid. This will allow us to make generalized statements on f dependence on R for all liquids.

Figure 2.6 presents f with respect to R for fixed mode number n. Drops of $n = 2$ are shown to be fundamentally different than typical Leidenfrost star oscillations reported here and will be discussed shortly in Section 2.6.1.

2.3.2 Shape irregularities

Typical oscillations reported here are for large amplitude star-shaped drops; however, as previously mentioned, some drops were atypical in both size and shape. The shape of these drops are more polygonal than star-shaped owing to a smaller amplitude of oscillation. In comparison to the typical star-shaped drops, these drops are observed to oscillate at higher f with smaller amplitude. In addition, these drops were found to be much smaller in R for a given mode number n than expected for

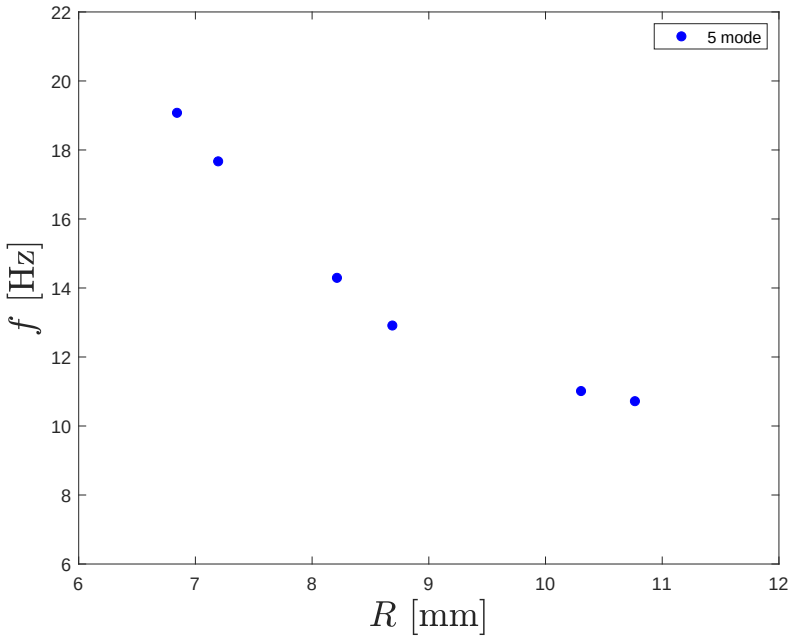

Figure 2.5: Oscillation frequency f against radius R for a single water drop exhibiting $n = 5$ oscillations over several minutes.

typical star oscillations. Drops of this nature are included in this study as they were fully developed oscillations.

Figure 2.7 distinguishes star and polygonal drops. Here we see water drops of $n = 4$ and $n = 6$ have the largest range of frequencies. In addition, there are two regions of concentrated frequency values for $n = 4$ and $n = 6$. As mentioned previously, the region of higher frequency values corresponds to smaller drops and lower frequency values correspond to larger drops. Water drops of $n = 4$ were observed with two distinct shapes either the typical star shape or a lower amplitude polygonal square shape. These shapes are shown in Figure 2.8 where the magenta marker from Figure 2.7 corresponds to a smaller square drop and the cyan marker for a larger star-shaped drop. The star drop has $R = 8.3$mm and $f = 12$Hz whereas the square drop has $R = 4.6$mm and $f = 28$Hz.

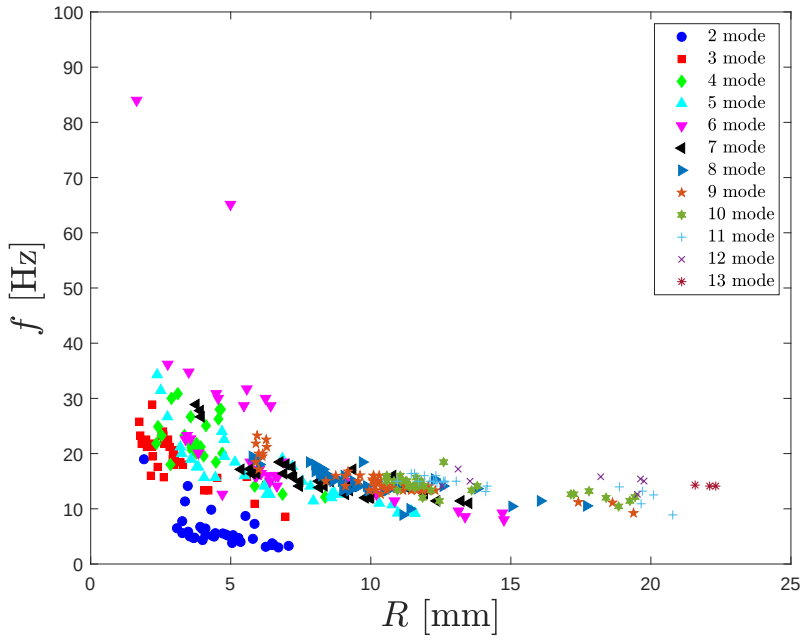

Figure 2.6: Oscillation frequency f against radius R for fixed mode number n.

Water drops of $n = 6$ were also observed with two distinct shapes; however, only a single observation is reported for a $n = 6$ sided polygon water drop. This drop corresponds to the highest frequency in Figure 2.7. Looking back at the two regions of concentrated frequency values, we see a similar trend for $n = 4$ drops. The main difference here is that small drops in the high frequency region are not polygonal as was the case for $n = 4$ drops. These drops are again much smaller in R yet remain star-shaped with no significant deviation from the typical star oscillations reported here. The general relationship between the f of these two regions for $n = 4$ and $n = 6$ is found for small drops to have roughly twice the f of larger drops. As shown for water, this same trend of higher frequency for smaller drops is found for all six liquids.

The smallest fully developed oscillating drop recorded was for a $n = 6$ polygonal liquid nitrogen drop which oscillated at the highest reported frequency of ap-

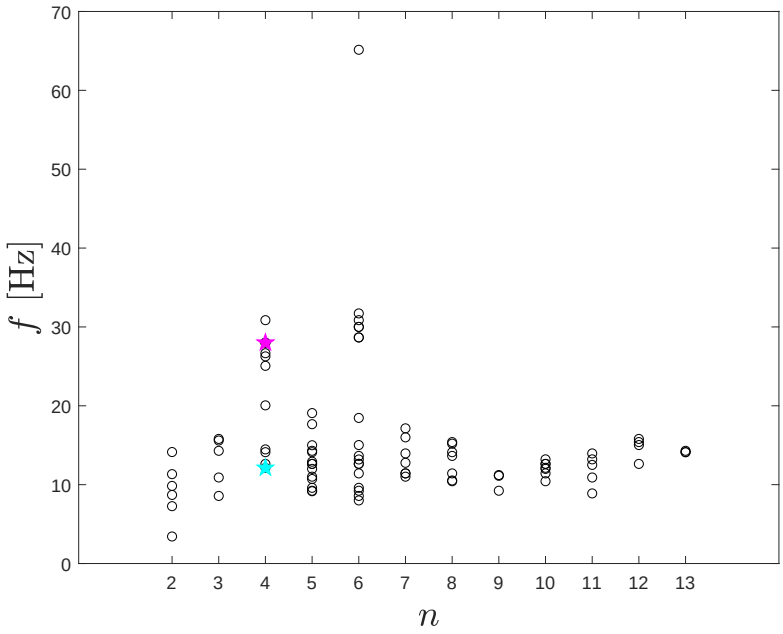

Figure 2.7: Oscillation frequency f against mode number n for water.

Figure 2.8: Frames taken during $n = 4$ oscillations of a water drop.

proximately 84 Hz. The two high frequency observations are shown in Figure 2.4 as the two uppermost markers to the far left. These oscillating drops possessed small amplitude and high frequency which made collecting data difficult due to imaging limitations, specifically the frame rate of the camera. The $n = 6$ liquid nitrogen drop is shown in Figure 2.9 where these low quality images are filtered in order to improve visualization of the polygonal drop periphery. Frames are taken one half period apart to illustrate their polygonal shape and small amplitude oscillating behavior. These drops are characteristically different than the typically observed Leidenfrost star oscillations due to their high frequency, low amplitude and relatively high mode number n for the given radius R.

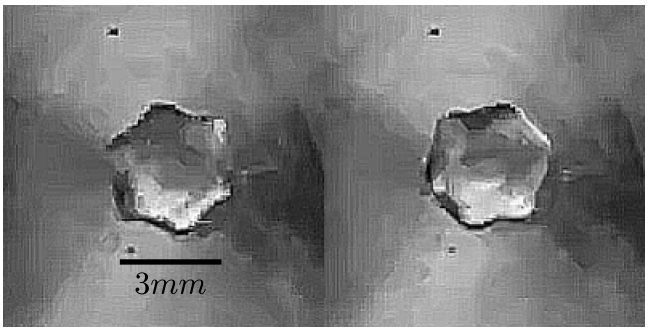

Figure 2.9: High freqency $n = 6$ oscillations of a liquid nitrogen drop. Frames taken one half period apart.

2.4 Mathematical model

To better understand the system dynamics governing drop oscillations in the Leidenfrost state, a mathematical model is derived to describe the surface oscillations. This is a simplified approach to elucidate the underlying physics of this complex dynamical system. The vapor flow and subsequent lubrication pressure, thermal

effects and surface geometry all dramatically influence the dynamics of the system. In order to simplify the problem, these aspects of the system will not be considered.

Figure 2.10 illustrates a top view of a Leidenfrost drop perturbed by ϵ about it's equilibrium radius R. The equilibrium radius R and perturbed radius r are specified from the center of the drop to the periphery of the equilibrium drop shape and to the perturbed drop shape respectively. η represents the surface shape of the perturbed drop along the drop periphery.

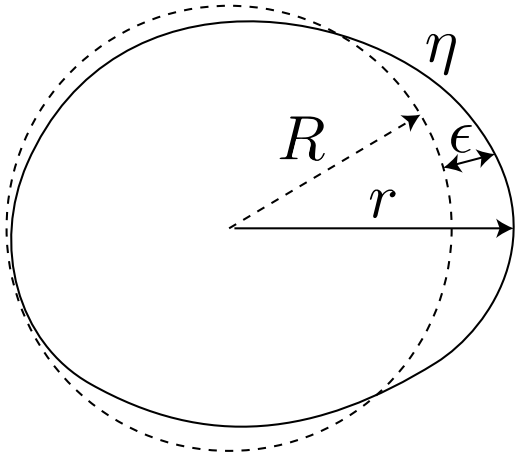

Figure 2.10: Schematic of a liquid drop perturbed about it's equilibrium shape. The dashed circle represents the equilibrium shape as viewed from above.

The simplified model is based on a 2-dimensional linear stability analysis of a drop perturbed about its equilibrium shape. The following analysis shows that a drop will oscillate with prescribed frequency about its circular equilibrium shape.

2.4.1 Field equations

A liquid drop perturbed about it's equilibrium shape is given in Figure 2.10. The radius, pressure and velocity of the perturbed drop are given by the following

$$r = R(1 + \epsilon\eta) \tag{2.1}$$

$$P = \overline{P} + \epsilon P^{'} \tag{2.2}$$

$$\boldsymbol{v} = 0 + \epsilon\nabla\phi \tag{2.3}$$

where the first term on the right hand side of equations 2.1-2.3 represent the equilibrium condition and the second second represents the first order perturbation correction response to a small perturbation ϵ. These are our disturbance equations which we now solve.

Consider an incompressible inviscid fluid with irrotational velocity field such that, the velocity field within the domain of the drop may be defined by the gradient of the velocity potential $\boldsymbol{v} = \nabla\phi$ where the velocity potential ϕ satisfies Laplace's equation in polar coordinates

$$\Delta\phi = \frac{1}{r}\frac{\partial}{\partial r}r\frac{\partial\phi}{\partial r} + \frac{1}{r^2}\frac{\partial^2\phi}{\partial\theta^2} = 0. \tag{2.4}$$

The kinematic boundary condition equates the radial fluid velocity at the interface to the velocity of the interface,

$$\frac{\partial\eta}{\partial t} = \left.\frac{\partial\phi}{\partial r}\right|_{r=R}. \tag{2.5}$$

Substituting the velocity field into the inviscid Navier-Stokes equation and keeping the lowest order terms results in the linearized Bernoulli equation

$$\rho \frac{\partial \phi}{\partial t} = -P. \tag{2.6}$$

The capillary pressure at the interface is given by the linearized Young-Laplace equation

$$P_{cap} = -\frac{\sigma}{R^2}\left(-\frac{\mathrm{d}^2\eta}{\mathrm{d}\theta^2} - \eta\right) \tag{2.7}$$

A solution is constructed using a normal mode analysis which assumes the surface disturbance takes the following form,

$$\eta(\theta, t) = \cos(n\theta)e^{i\omega t}. \tag{2.8}$$

2.4.2 Solution method

We need to construct the associated solution to Laplace's equation, which we assume to be separable and non-singular at the origin $r = 0$. The general solution to Laplace's equation in 2D polar coordinates is well-known and we use the kinematic boundary condition (2.5) to specify the Fourier coefficients to yield the velocity potential

$$\phi(r, \theta, t) = i\omega \frac{R}{n}\left(\frac{r}{R}\right)^n \cos(n\theta)e^{i\omega t} \tag{2.9}$$

Lastly, we equate the capillary pressure with the fluid pressure at the interface and solve for the angular frequency ω in rad/s. Converting to Hertz leaves us with the drop oscillation frequency f_m in Hertz concluding this model.

$$f_m = \frac{1}{2\pi}\sqrt{\frac{\sigma n(n^2-1)}{\rho R^3}} \tag{2.10}$$

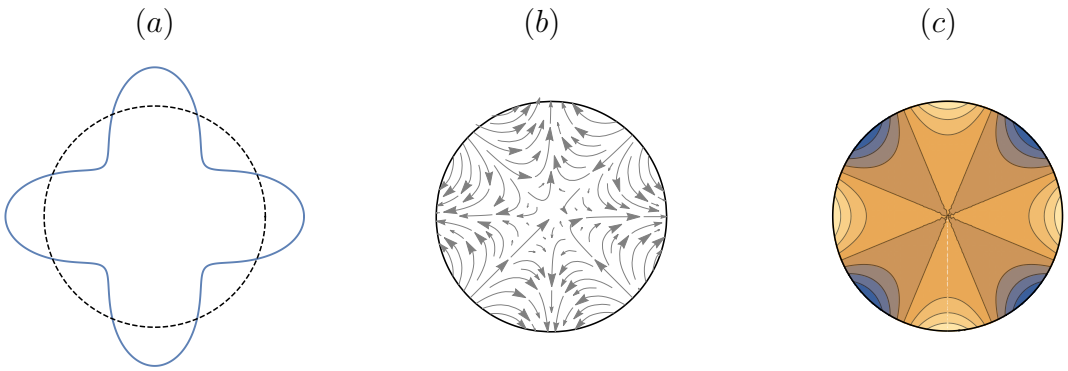

Figure 2.11: Solutons for the (a) surface shape, (b) velocity field and (c) pressure field of a perturbed $n = 4$ liquid drop.

Solutions are given for the surface shape in Figure 2.11 (a), velocity field in Figure 2.11 (b), and pressure field in Figure 2.11 (c) for an $n = 4$ drop. The dashed circle in Figure 2.11 (a) represents the equilibrium drop shape and blue represents regions of higher pressure in Figure 2.11 (c).

2.5 Scaled data

In this section, we introduce a frequency scaling based on the provided mathematical model in Section 2.4. We also adopt a scaling in R based on the fluid properties, namely capillary length l_c. This is a typical scaling used when describing small drops isolated from their surroundings (Aussillous and Quéré, 2001, 2006; Quéré, 2013; Soto, 2014; Ma et al., 2017).

2.5.1 Scaling

In order to quantitatively compare oscillating drops of all liquid types we may modify Figure 2.4 with an adopted scaling. The idea is to scale drop radius R

with each liquid's capillary length l_c in order to make generalized statements on f dependence on R for all liquids. This scaling collapses the data in R for all liquids. Figure 2.12 presents f as a function of scaled radius R/l_c. We can now clearly see the distinction between small and large liquid nitrogen drops. The largest oscillating drops are observed to have radii around $9l_c$ while the smallest drops have a radius just larger then l_c in agreement with Ma and Burton (2018). Oscillating drops of this size are made possible with the curvature imposed on the substrate surface (Snoeijer et al., 2009). Figure 2.13 presents the same data sorted by mode number n. Here we can clearly see that drops of $n = 2$ are fundamentally different than typical oscillations reported here. These oscillating drops were observed over a large range of R/l_c and have relatively low f than all other reported oscillations. The $n = 2$ oscillations will be further discussed in Section 2.6.1. The confidence intervals for the data in Figure 2.13 are presented in Figure 2.14 where again the $n = 2$ oscillations are shown to be atypical of Leidenfrost star oscillations.

There is some disagreement on whether oscillation frequency is dependent on drop radius (Snezhko et al., 2008; Bouwhuis et al., 2013; Caswell, 2014; Ma et al., 2017; Brunet, 2018). Here, we clarify this dependence by characterizing drops into two regimes based on radius R and capillary length l_c. Figure 2.15 presents f as a function of R where each liquid is catagorized into one of two regimes based on the value of scaled radius R/l_c. The two regimes are $R/l_c < 4$ and $R/l_c > 4$. We do not consider the large amplitude $n = 2$ oscillations as they were shown to be fundamentally different than typical Leidenfrost star oscillations. The oscillation frequency of drops $R/l_c < 4$ are shown to vary nonmonotonically in R. Drops of $R/l_c > 4$ are shown in Figure 2.15 to have a single constant frequency for each liquid largely independent of radius R and mode number n. The approximate oscillation frequency for drops of $R/l_c > 4$ is 12 Hz for water, 14 Hz for acetone, 15 Hz for

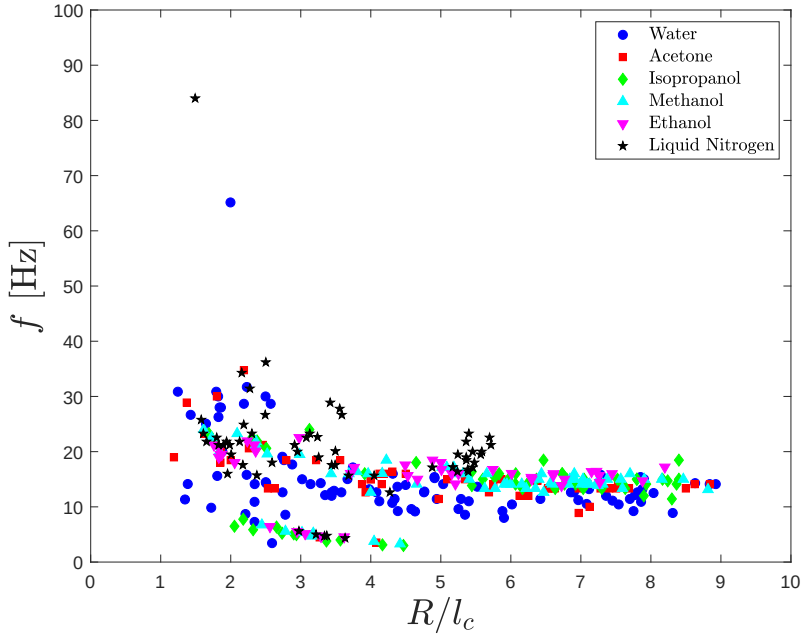

Figure 2.12: f as a function of R/l_c

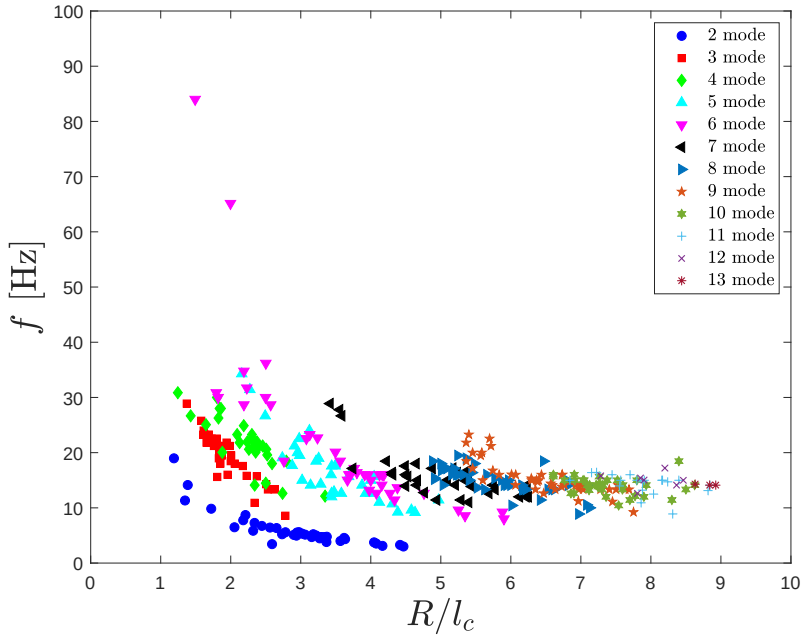

Figure 2.13: Oscillation frequency f plotted against scaled radius R/l_c for fixed mode number n.

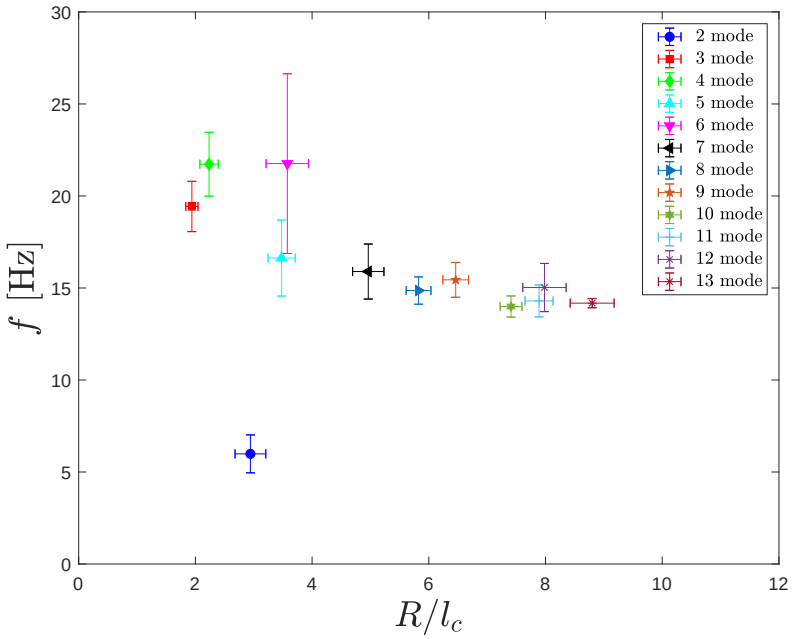

Figure 2.14: Oscillation frequency f plotted against radius scaled radius R/l_c for fixed mode number n. Error bars correspond to 95% confidence intervals.

isopropanol, 15 Hz for methanol, 16 Hz for ethanol and 18 Hz for liquid nitrogen. This is largely in agreement with Ma and Burton (2018) who found a constant freqeuncy for water, acetone, isopropanol, methanol and ethanol to be roughly 14 Hz and a constant frequency for liquid nitrogen to be roughly 17 Hz.

Introducing the frequency scaling found from equation 2.10 in addition to the scaled radius R/l_c allows the data to collapse in both the horizontal and now the vertical as well and is presented in Figure 2.16 for each mode number n. The data collapses adequately with this scaling leading to the conclusion that these oscillations are in fact capillary oscillations as predicted by Rayleigh (1879), specifically as predicted by equation 2.10 governing the simplified model outlined in Section 2.4. The 95% confidence intervals for the scaled frequency and scaled radius in Figure 2.16 are presented in Figure 2.17. A horizontal line is drawn at $f/f_m = .75$ to show the

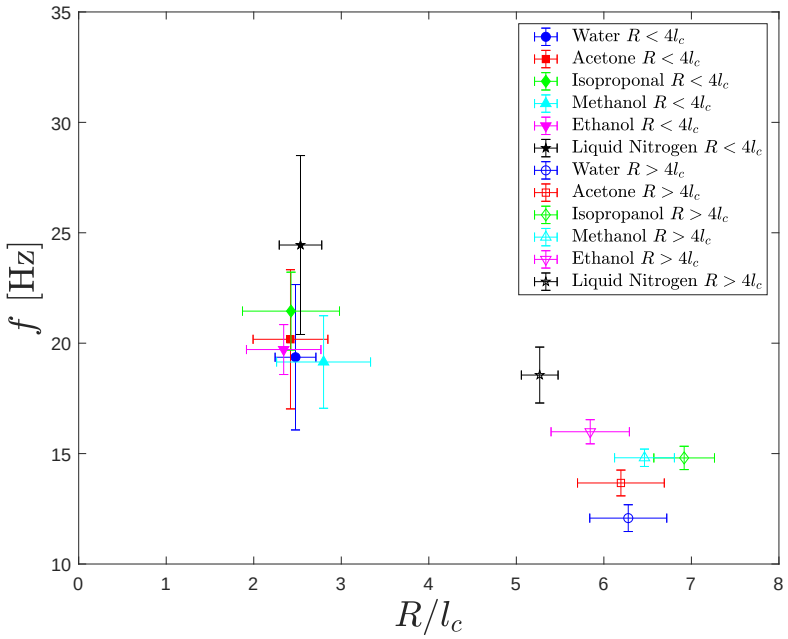

Figure 2.15: Oscillation frequency regimes $R < 4l_c$ and $R > 4l_c$ for each liquid.

average of this value across all modes.

Courty et al. (2006) provides a correction factor to the Rayleigh frequency based on spherical harmonics appearing in the solution to Laplace's equation in spherical coordinates for forced oscillations at a point.

$$f_{Courty} = \frac{1}{2\pi}\sqrt{\frac{\sigma n(n-1)(n+2)}{\rho R^3\left(1+\sqrt{\frac{2n+1}{4\pi}}\right)}} \tag{2.11}$$

We scale our experimental data with the model frequency found by Courty et al. (2006). Figure 2.18 presents this scaling. This scaling is found to agree better to experimental data; however, with a slight dependence on R as is shown by the upward sloping trend in scaled frequency f/f_{Courty} over scaled radius R/l_c.

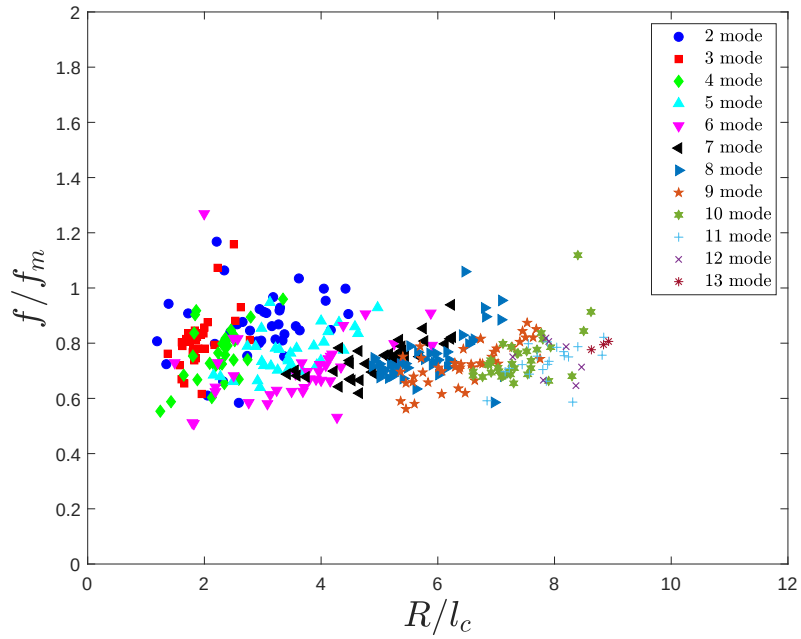

Figure 2.16: Scaled oscillation frequency f/f_m of each mode number plotted against scaled radius R/l_c.

2.6 Complex dynamics

Several peculiar observations on the complex motion of oscillating Leidenfrost drops are reported here. We discuss mode selection, specifically the atypical $n = 2$ oscillations mentioned in the previous section. We also show observations of mode doubling and a hydrodynamic instability caused by rising vapor. Finally we discuss the mechanics of Leidenfrost drop oscillations.

2.6.1 Mode number selection

Generally, mode number n is observed to decrease with decreasing drop size during vaporization. This may be understood as decreasing drop circumference restricts the perimeter on which capillary waves of characteristic wavelength may pro-

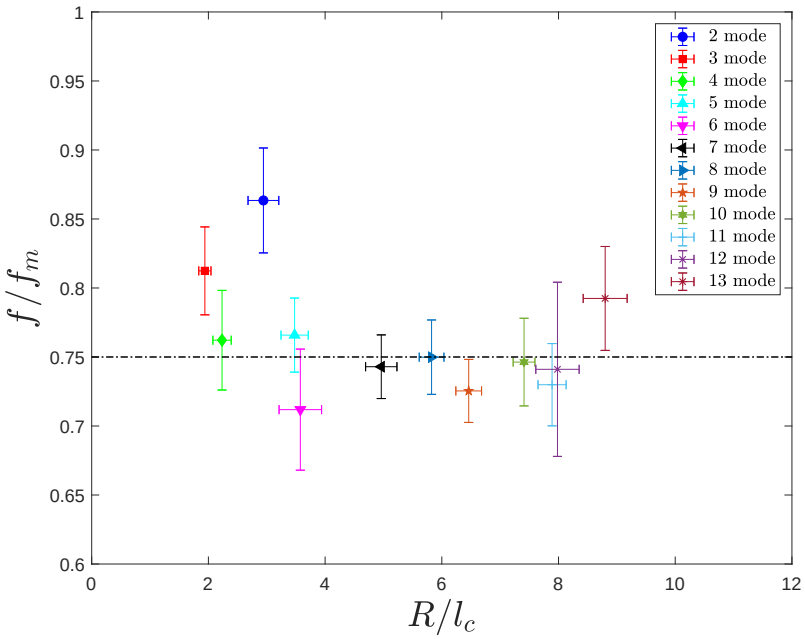

Figure 2.17: Scaled oscillation frequency f/f_m plotted against scaled radius R/l_c for fixed mode number n.

pogate. Water was generally observed to undergo sequential mode reduction quite regularly in comparison to the other liquids; however, skipping of modes was also frequently observed.

The mode number n of Leidenfrost drops is essentially set by the circumference of the drop; however this is not strictly true as will be discussed. For a given radius R we expect a mode number n corresponding to that particular R. Instead we observe a range of n for a given R. Further study on mode transition is needed to make any definitive statements; however for now we may say that for a given drop radius R we expect a range of mode numbers n which are selected by the dynamics of the system. Figure 2.19 which plots modes number n against radius R clearly shows that $n = 5, 6, 7$ are all possible modes that may be selected by the dynamics of the system for a water drop of $R = 10$mm for example.

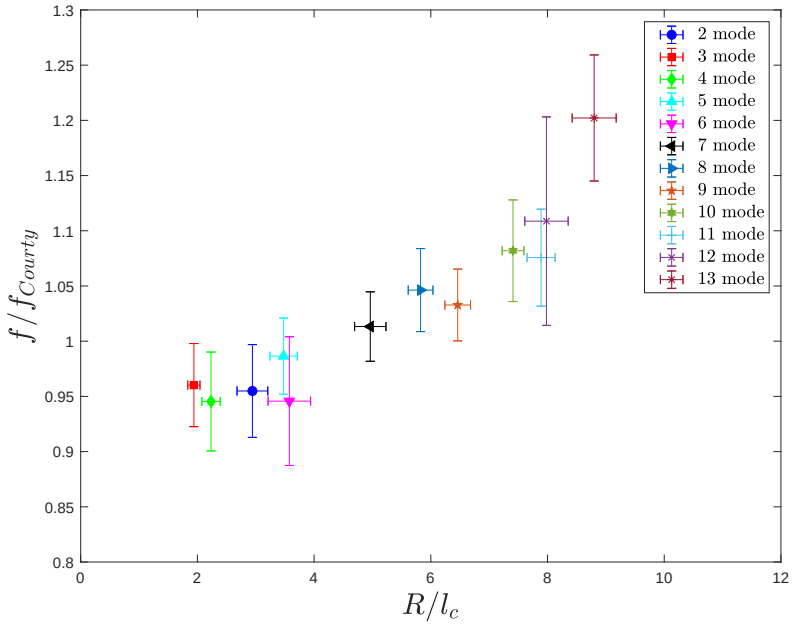

Figure 2.18: Scaled oscillation frequency f/f_{Courty} plotted against scaled radius R/l_c for fixed mode number n.

For drops of acetone, isopropanol, methanol, ethanol and liquid nitrogen fully developed $n = 2$ oscillations were observed over a considerably large range of radii. For these liquids, $n = 2$ was observed to be the preferred mode where typically higher modes would be expected for this range of drop radii. This dominant mode of oscillation was much larger in amplitude than the typical star oscillations reported here. The range of radii for these large $n = 2$ drops is shown in Figure 2.20 where isopropanol is shown to cover a range of R from 3 mm to 7 mm. Higher modes are typically expected for these larger radii drops as shown by the gap in data for $n = 4$ and $n = 5$ excluding the blue markers. The radius of these large $n = 2$ drops was generally consistent with an expected higher mode of oscillation. It is believed that a range of mode numbers are not preferred by the dynamics of the system and subsequently $n = 2$ is the preferred state of the system. It should be noted that the

only other mode observed in this range was a single $n = 6$ drop which was an instance of mode doubling which will be discussed shortly in Section 2.6.2.

In order to excite modes other than $n = 2$ over this range of radii, we construct a substrate with a geometry targeted for this purpose. A shallow circular depression is machined into the surface of a flat plate. The radius of this depression is selected specifically to be within the range of expected radii for $n = 4$ and $n = 5$ drops. This allowed for $n = 4$ and $n = 5$ drops to be induced; however, these oscillations were generally more disordered than typical star oscillations. The blue markers represent experiments run with surface geometry targeted to induce $n = 4$ and $n = 5$ modes.

As mentioned previously, mode transitions were not strictly limited to reduction in mode number n as many of these large amplitude $n = 2$ drops would transition to $n = 3$ for a brief moment before assuming the static shape discussed previously. Drops of higher mode number n were rarely observed to increase in mode number during drop vaporization; however, this was still observed on a few occasions.

Figure 2.21 presents a single term power law fit to $n = 2$ isopropanol oscillations. A power law fit was performed for isopropanol $n = 2$ drop due to the large number of observations of this mode over a relatively large range of R in comparison to the other liquids exhibiting these atypical large amplitude $n = 2$ oscillations. From this fit, the frequency of these large $n = 2$ drops is found to correlate to $R^{-1.11}$ rather than $R^{-1.5}$ as expected from Equation 2.10.

These large amplitude $n = 2$ drops are characterized by their relatively low f and the observation of these drop over a relatively large range of R. Figure 2.22 shows a typical large amplitude $n = 2$ isopropanol drop undergoing reduction in radius during vaporization, frames are taken one half period apart to show oscillatory motion. During this reduction in radius modal transitions are observed. Frames 1 and 2 show the typical large amplitude $n = 2$ oscillation at 4.29 Hz. In frames 3 and

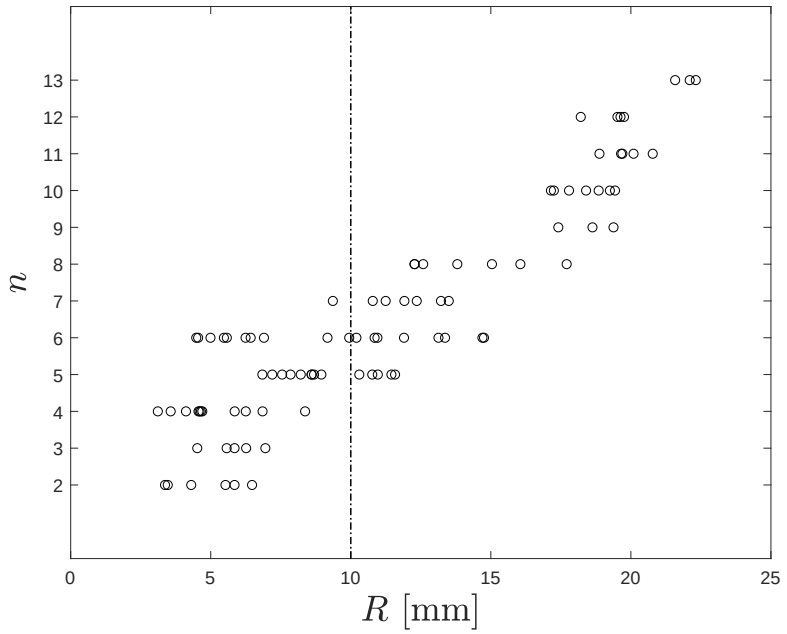

Figure 2.19: Mode n dependence on radius R for Water.

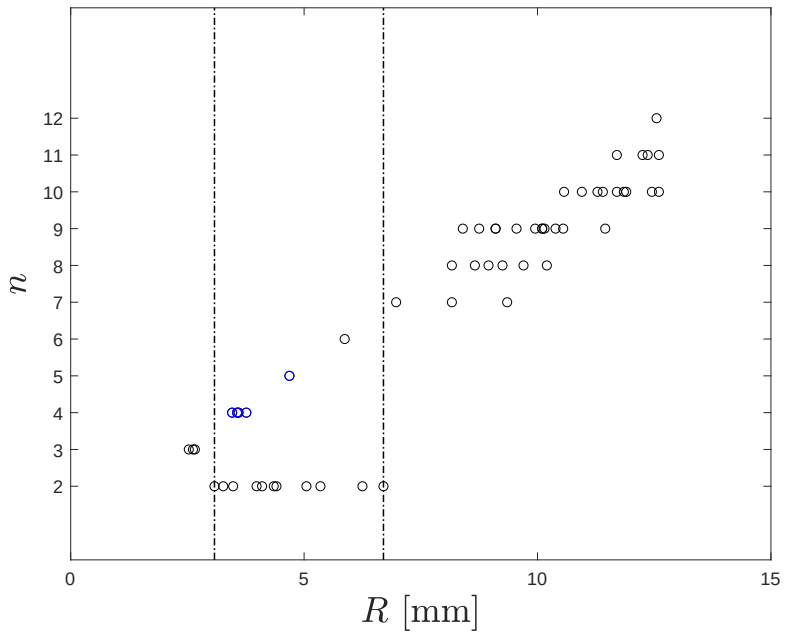

Figure 2.20: Mode n dependence on radius R for Isopropanol.

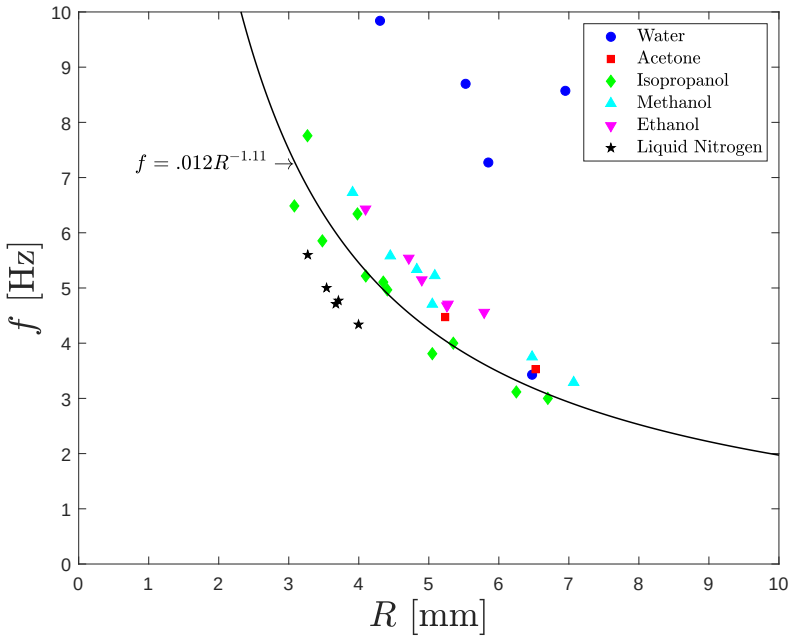

Figure 2.21: Power law fit on isopropanol $n = 2$ oscillations.

4 we shown an incomplete development of another mode, possibly $n = 3$, however this mode is quickly damped and the preferred $n = 2$ mode resumes in Frames 5 and 6. Here we show the relative reduction in radius from frames 1 and 2 now at 7.5 Hz. Finally frames 7 and 8 shown the transition into $n = 3$ at 20 Hz. This sequence of mode transition was typical of isopropanol and ethanol.

We average the data for each mode in both f and R and apply confidence intervals in Figure 2.23 to further demonstrate that these $n = 2$ oscillations are in fact fundamentally different than the typically observed Leidenfrost star oscillations. As shown by the averaged data and confidence intervals, the $n = 2$ oscillations are shown to deviate significantly from the typical f encountered in these Leidenfrost star oscillations.

The effect of amplitude ϵ on oscillation frequency f has been explored by Tsamopoulos and Brown (1983) who provided amplitude correction factors for oscil-

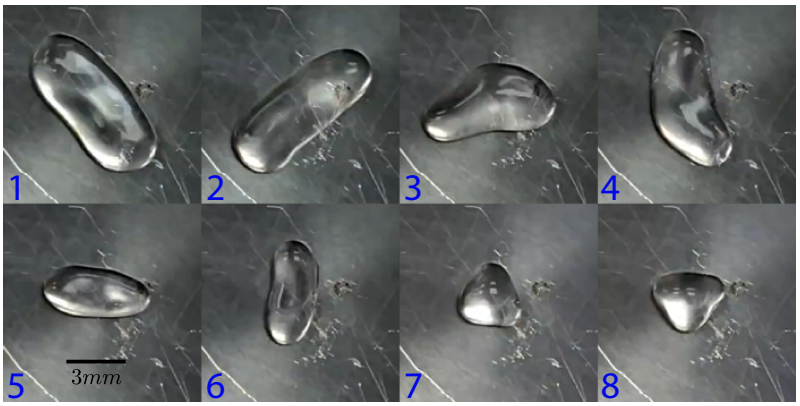

Figure 2.22: Large amplitude $n = 2$ isopropanol drop undergoing radius reduction and mode transition.

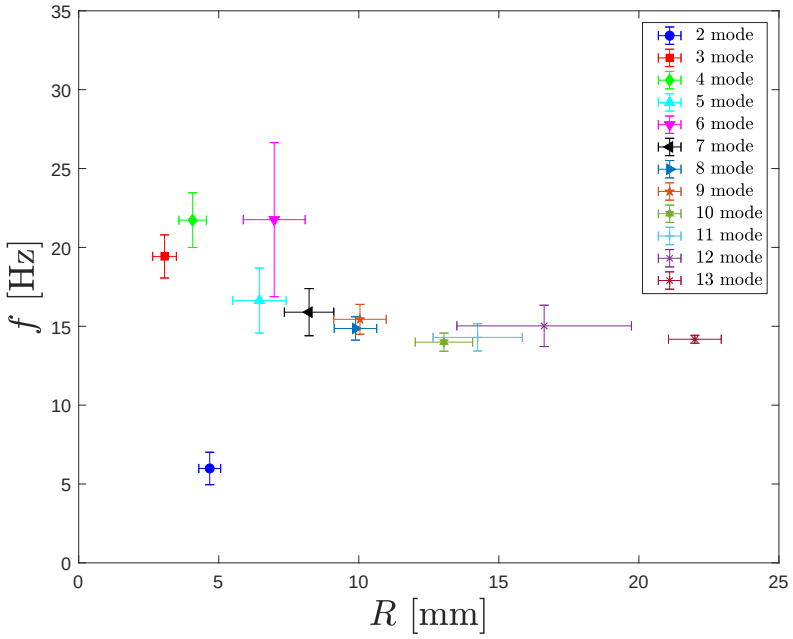

Figure 2.23: Oscillation frequency f plotted against radius R for fixed mode number n. Error bars correspond to 95% confidence intervals.

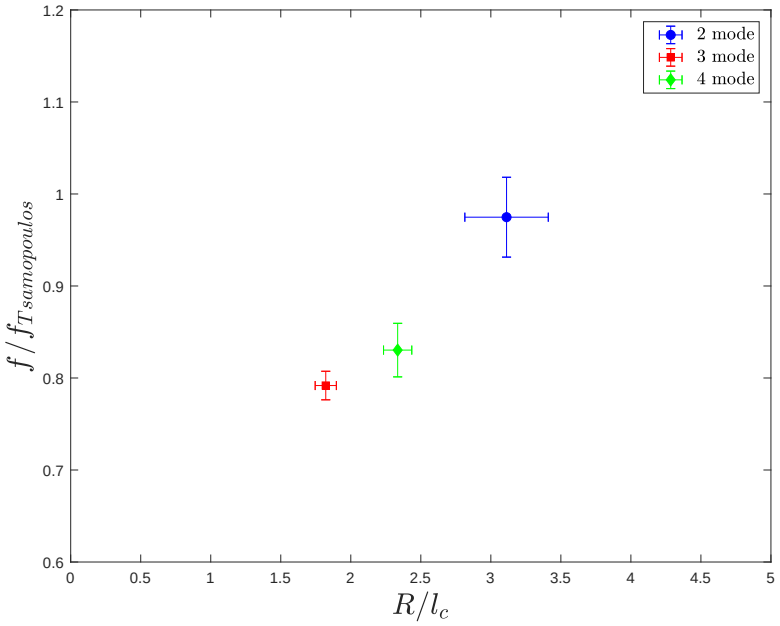

Figure 2.24: Scaled frequency $f/f_{Tsamopoulos}$ plotted against scaled radius R/l_c for mode numbers $n = 2 - 4$.

lation mode numbers $n = 2-4$. Figure 2.24 shows our experimental data for $n = 2-4$ scaled by this corrected frequency. Oscillation frequency f is shown to collapse well for the large amplitude $n = 2$ oscillations.

2.6.2 Mode doubling

Here we report the first observation of two modes appearing simultaneously during Leidenfrost star oscillations. The combination of two modes appearing during fully developed oscillations was observed several times. We term this phenomenon mode doubling. Mode doubling was observed with the typical star oscillations around the drop periphery of mode number n in addition to lower frequency oscillations of the overall drop shape at a lower mode number m. Figure 2.25 shows a water drop exhibiting $n = 5$, $m = 2$ mode doubling. The typical $n = 5$ star oscillation is shown

in the red frames and the low frequency $m = 2$ mode oscillation is shown in the blues frames. Observations of mode doubling are summarized in Table 2.3. Rotating large polygons of $n = 2$ up to $n = 5$ sides were also observed for large unorganized oscillating Leidenfrost drops where the radial outward vapor flow beneath the drops is speculated to generate significant shear stress disrupting the typical star oscillations (Snoeijer et al., 2009). Interestingly, the higher frequency n star oscillations are found to be approximately four times higher than the lower frequency m oscillations as illustrated in Figure 2.25 and shown for all other mode doubling observations in Table 2.3 possibly alluding to lower harmonics.

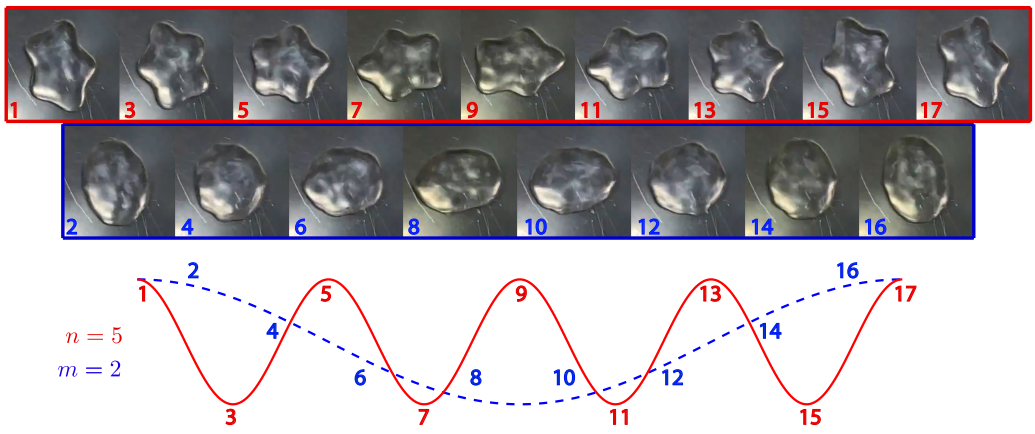

Figure 2.25: Timetrace of a water drop presenting $n - m = 5 - 2$ mode doubling over a single period for the low frequency $m = 2$ mode oscillation and 4 periods for the typical $n = 5$ oscillation.

2.6.3 Rayleigh-Taylor type instability

An inverse Rayleigh-Taylor type instability is reported for Leidenfrost drops in which the flowing vapor beneath the drop is unable to completely escape radially from underneath the drop. This increases the pressure underneath the drop until eventually a vapor pocket grows unstable and bubbles begin rising due to buoyancy

Liquid	$n-m$	n-frequency	m-frequency	frequency ratio (n/m)
Water	$5-2$	15.33	3.93	3.90
	$5-2$	13.59	3.67	3.70
Isopropanol	$6-2$	17.58	4.06	4.33
	$7-2$	17.58	3.88	4.53
Methanol	$11-3$	13.36	3.29	4.06
Ethanol	$12-3$	17.14	3.88	4.42
	$11-3$	17.14	4.92	3.49
	$11-3$	16.76	4.51	3.72
Liquid Nitrogen	$6-2$	30	6.41	4.68

Table 2.3: Observations of mode doubling

forces eventually breaking through the overlying liquid surface.

This instability can be characterized by vapor bubbles originating in the vapor pocket below the drops rising through the liquid eventually breaking the top surface of the drop leaving an unstable torus configuration of the drop shape before this torus closes and the next vapor pocket begins to develop. A timetrace of this instability manifesting in a liquid nitrogen drop for a single bubble breakthrough is provided in Figure 2.26.

One peculiar observation of this instability is the fact that, while typically detrimental to the fully developed star oscillations, this instability also generated strong oscillations with greater amplitude than the typical star oscillations. These oscillations however, are caused by the rising vapor bubbles which were not uniformly periodic and thus the oscillations were not well self-reinforced. The liquid rebounds while displaying strong unorganized oscillations back to the center until the next rising bubble breaks the upper liquid surface. This instability can be referred to as a type of inverse Rayleigh-Taylor instability. A timetrace of a methanol drop displaying these strong oscillations of $n = 4$ drop during the RT instability showing the rising vapor bubbles is provided in Figure 2.27. Strong oscillations during this instability

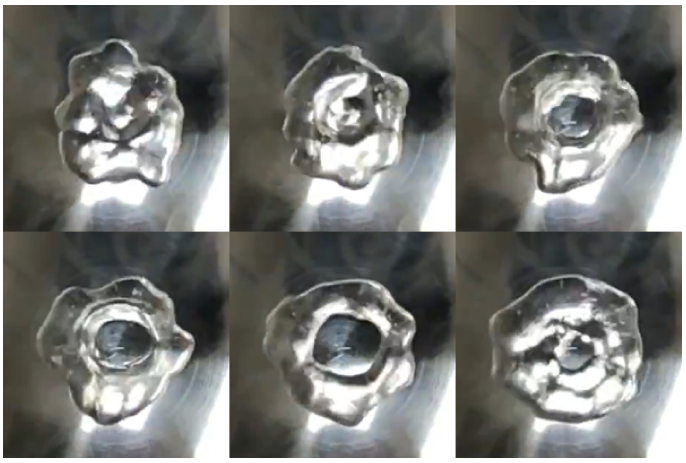

Figure 2.26: Timetrace of a liquid nitrogen drop exhibiting the inverse Rayleigh-Taylor instability over two complete vapor bubble breakthroughs.

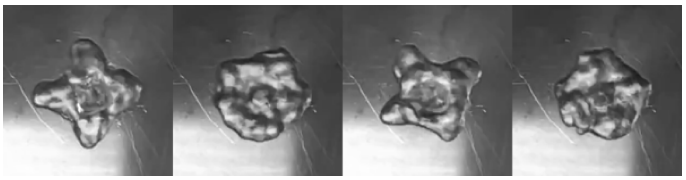

Figure 2.27: Timetrace of a methanol drop exhibiting strong $n = 4$ oscillations during the inverse Rayleigh-Taylor instability.

were observed for mode numbers $n = 2 - 4$.

2.6.4 Mechanics of star oscillations

Shear stress developed on an interface between two fluids moving at different velocities has been known to induce interfacial capillary waves (Miles, 1957; Zhang, 1995; Chang and Demekhin, 2002; Zeisel et al., 2008; Paquier et al., 2015). It is also known that underneath Leidenfrost drops, there is significant radial flow of the vapor outward from the center of the drop Holter and Glasscock (1952); Gottfried

et al. (1966); Adachi and Takaki (1984); Avedisian and Koplik (1987); Biance et al. (2003); Quéré (2013). Snoeijer et al. (2009) finds that large amplitude oscillations cannot occur from only considering viscous lubrication and capillary effects of the flow under the drop and speculates that inertial effects play a role in the spontaneous oscillations. They suggest that large amplitude oscillations occur when inertia in the flow underneath the drop is significant. Viscous shear stress generated at the liquid-vapor interface leading to a Kelvin-Helmholtz type instability inducing characteristic capillary waves underneath the drop has been proposed as a mechanism for the spontaneous occurrence of the observed star oscillations Adachi and Takaki (1984). Ma et al. (2017) found pressure fluctuations in the vapor layer with a frequency approximately twice that of the star oscillations. Ma and Burton (2018) speculates that a Kelvin-Helmholtz type instability due to the shear stress generated by the vapor flow may give rise to capillary waves of a characteristic length underneath Leidenfrost drops. They propose that these capillary waves lead to variations in the vapor layer thickness causing the observed pressure fluctuations in the vapor layer, ultimately concluding that the pressure fluctuations act as a parametric forcing mechanism for the appearance of the star oscillations (Miles and Henderson, 1990). However, the authors also note that this variation in the vapor layer thickness could be caused by the vertical motion of the drop center of mass and that pressure fluctuations could instead be caused by the oscillations themselves.

We also observe waves forming underneath Leidenfrost drops propogating from the center outward radially. These waves are observed to become polygonal corresponding to mode number n. Figure 2.28 clearly shows this wave appearing at first polygonal during a vanishing low amplitude $n = 6$ oscillation then becoming circular as the drop assumes the static equilibrium shape. These waves were observed for many Leidenfrost drops and typically would preceed star oscillations. However,

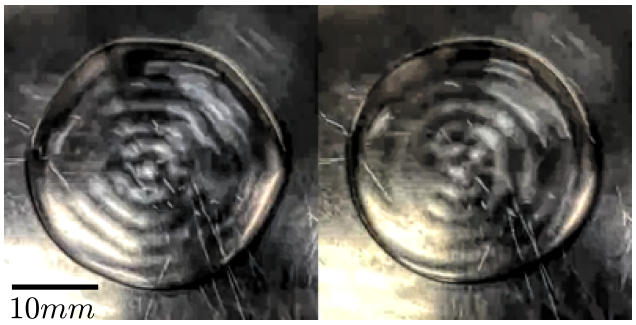

Figure 2.28: Wave propogating radially outward underneath a water drop. Contrast modified for better visualization.

this wave was observed several times without the appearance of star oscillations. We believe this wave appearing underneath Leidenfrost drops plays a role in the development of the star oscillations. Typically these waves were visible on smaller drops and even on the top surface of the drop exhibited this wave feature.

Brunet and Snoeijer (2011) concludes that these oscillations originate from periodic temporal fluctuations of the drop radius. They found that star oscillations occur above a critical Reynolds number of roughly 10 in the vapor flow. They concluded that star oscillations appear when the center of mass of the drop vibrates vertically with sufficient amplitude. They speculated that star oscillations may be allowed by the deformation allowed by a liquid or possibly influenced by internal flows. They also speculated that a high liquid drop viscosity could damp these oscillations. Bouwhuis et al. (2013) also finds that star oscillations result from a parametric excitation which only occurs for low viscosity fluids. However, we have observed $n = 2$ and $n = 3$ large amplitude oscillations of a water-glycerol solution and believe future investigations may focused on understanding the effect of viscosity on Leidenfrost star oscillations.

Bouwhuis et al. (2013) found that for high viscosity drops, only the breathing mode may exist. This breathing mode has been proposed as a mechanism for star oscillations Caswell (2014) who found this to be coupled to and $\pi/2$ out of phase with the known vertical oscillation motion of drops. This breathing mode is found to scale differently than the Rayleigh frequency. Caswell (2014) fits a power law with a frequency dependence of $R^{-0.68}$. The mechanism behind this breathing mode and the associated scaling found by Caswell (2014) is unknown. Ma and Burton (2018) provided an analytical model describing this breathing mode.

We leave the investigation on the origin of spontaneously oscillating Leidenfrost drops to future studies. We believe future studies could be geared toward the exploration of substrate geometry and its overall effect on mode selection as we showed here that substrate geometry is paramount in the mode selection process.

Chapter 3

Toroidal drops

As discussed in Section 1, substrate geometry significantly influences Leidenfrost drop dynamics. In this chapter, we explore this geometric dependence experimentally using several substrates of various geometry. Experimental results are provided and interpretations are given to quantify the geometric influence of substrate geometry on Leidenfrost drop dynamics. Several concepts introduced and discussed in Sections 1 and 2 will be referenced for brevity.

In order to investigate the geometric dependence on the dynamic response of Leidenfrost drops we construct several substrates intended to induce surface instabilities which can be experimentally quantified. This requires the suppression of instabilities known to be detrimental to experiment such as the Rayleigh-Taylor instability discussed in Section 1.4.2. Therefore, substrates must provide an easily accessible path for the vapor flow to escape from underneath the drop. As the vapor flow is believed to significantly influence drop dynamics and ultimately cause surface instabilities (Snoeijer et al., 2009), substrates are specifically designed to control the direction of vapor flow. In Section 2, the vapor flow u is directed radially outward from the center of each drop. As we believe the vapor flow to play a significant role

in the appearance of star oscillations along the periphery of the drop where the vapor exits, we speculate that directing the vapor flow to exit from under any free liquid surface will cause surface instabilities there. Therefore, the substrate geometries explored here are designed to direct the majority of vapor flow to exit beneath a free liquid surface.

Recently, Perrard et al. (2012) used unique substrate geometry where they found polygonal waves propagating along the surface of a liquid ring in the Leidenfrost state. These waves are much longer in wavelength than the star oscillations reported in Section 2. Following this, the goal of this chapter is to excite surface instabilities like these polygonal waves on a volume of liquid in the toroidal configuration.

3.1 Experiment

3.1.1 Experimental setup

We use the same experimental setup as depicted in Section 2.2.1. The only difference here is substrate geometry. We design two substrate geometries to confine large volumes of liquid in toroidal configurations. Each substrate is constructed from 360 brass which is considered to be largely isothermal as discussed in Section 1.3.

The first substrate uses a small radius of curvature along the outer edge to set the outer radius R_o of the liquid tori with a gradual constant 5° degree slope up and inward to the center as shown in Figure 3.1. Here the vapor flow u escapes radially inward up the constant slope. We call this substrate the torus plate. Two torus plates are constructed with the same geometry only scaled in size. Each plate is designed with a characteristic radius R_T which is a measure from the center of the plate to the deepest point in the torus trough. The small plate has $R_T = 30$mm and

the large plate $R_T = 50$mm. The geometry of the liquid tori is described in terms of its outer radius R_o and inner radius R_i which defines the torus width W where $W = R_o - R_i$. Due to the steep outer curvature on each torus plate, R_o is essentially constant for each torus plate size. R_i depends on the volume of liquid deposited onto the substrate surface, thus R_i decreases for larger volumes of water.

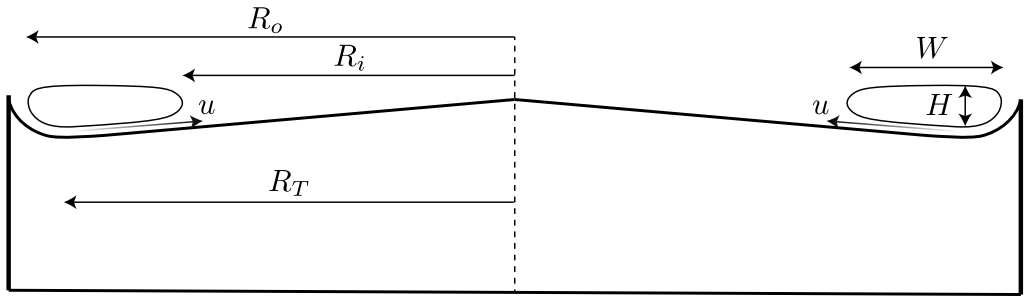

Figure 3.1: Illustration of the torus plate.

The second substrate sets the inner radius R_i of the liquid torus with a gradual constant 5° degree slope up and outward from the substrate center as shown in Figure 3.2. We call this substrate the inverted torus plate. This plate is designed with characteristic radius $R_T = 15$mm. Again, we define torus width W from the outer radius R_o and inner radius R_i where $W = R_o - R_i$. R_i is nearly constant for all liquid tori on the inverted torus plate with R_o increasing with larger volumes of liquid.

To control heating of the substrate, we use a Thermo-Scientific Super-Nuova hotplate to impose surface temperatures at the bottom of the substrate up to 723 K. The substrate is leveled on the hotplate with a DXL3605 Dual Axis Digital Angle Protractor with a resolution of 0.01°. Substrates are leveled to within .1° in each direction before each experiment. We deposit liquid onto the substrate surface using B+D syringes and image the liquid tori from above the substrate using a 12 megapixel camera. We also find it helpful to inject a constant stream of liquid using a motorized

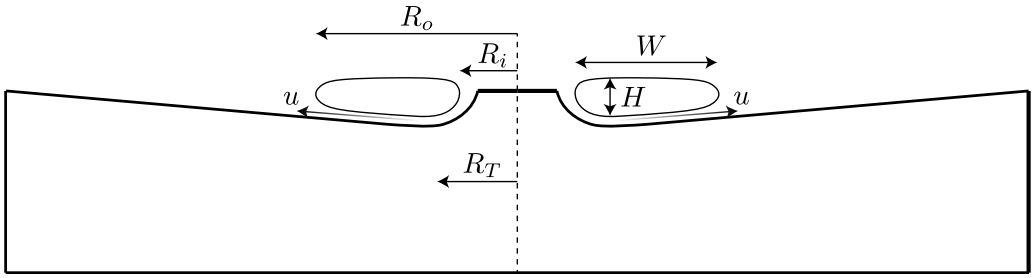

Figure 3.2: Illustration of the inverted torus plate.

syringe pump into the levitated torus in order to account for the vaporization occuring at the bottom liquid surface. We are able to match the vaporization rate with the injection rate ensuring a nearly constant volume of liquid during experiments. All experiments are conducted using preheated distilled water with properties from Lemmon et al. (2011) given in table 2.1 as the water is assumed to be just below its boiling temperature (Boutigny, 1843).

3.1.2 Experimental method

Substrates are heated beyond the Leidenfrost temperature for water inducing the Leidenfrost state upon deposition. A syringe is used to manually deposit preheated water onto the hot surface. Liquid preheating ensures the bulk liquid temperature remains just below the boiling temperature. To compensate for vaporization of the initial liquid volume, a motorized syringe pump is used to inject a constant flow into the liquid torus. With the liquid in the prescribed torus configuration, we record videos from above the substrate.

Videos are analyzed frame-by-frame using Adobe Premiere Pro CC software in order to measure the angular velocity ω of the wave propagating along the inner torus surface. To do this, we record the number of frames required for one complete rotation

and divide this from the frame rate of the camera to find ω in rad/s. Images are exported and processed using the NIH ImageJ software application to calculate torus width W from R_i and R_o in addition to recording the mode number n corresponding to the number of sides of the polygonal shape. We calculate wave propagation speed V in mm/s using $V = \omega R_i$. An average wavelength λ in mm is calculated from $\lambda = 2\pi R_i/n$.

3.2 Experimental results

3.2.1 Torus plate

Figure 3.3 shows the equilibrium toroidal configuration of water on the torus plate. These drops vary in width W depending on the volume of water and the size of the torus plate. The inner radius R_i is set by the volume of liquid for each plate size R_T. Torus height H is limited by $2l_c$ (Biance et al., 2003; Perrard et al., 2012; Quéré, 2013).

Figure 3.3: Static equilibrium toroidal shape on torus plate.

We observe polygonal waves propagating along the inner torus radius R_i at a

constant velocity. We report 35 observations of polygonal waves with number of sides $n = 3 - 14$, as shown in Figure 3.4.

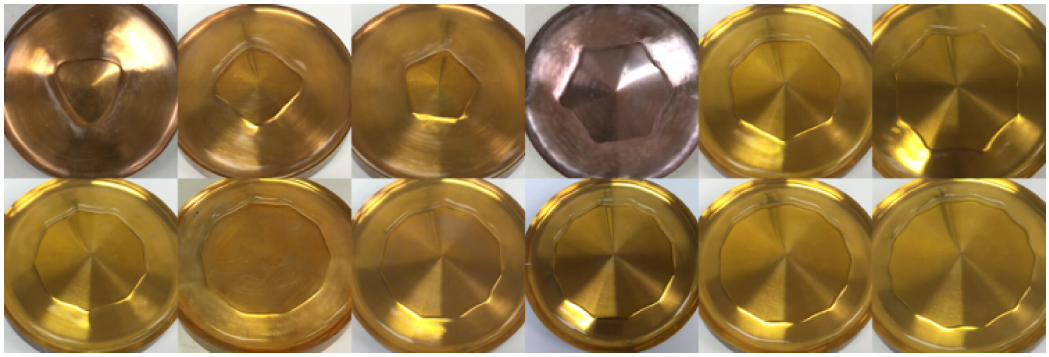

Figure 3.4: Polygonal wave propagating along inner torus surface for $n = 3 - 14$.

Figure 3.5 plots wave propagation speed V against mode number n. Error bars represent 95% confidence intervals. The propagating wave is found to have a nearly constant speed of $V \approx 95$mm/s irrespective of mode number, which agrees with Perrard et al. (2012).

The toroidal shape is characterized by an aspect ratio W/R_T. Figure 3.6 shows the mode number n decreases with aspect ratio W/R_T, similar to Perrard et al. (2012). However, we also observed several waves propagating with wavelength λ longer than typically reported. We begin to see the same trend for these longer wavelengths in Figure 3.6; however, more experimental data is needed to confirm this observation. Oddly we find for even n more concentrated data and for odd n more dispersed data although this could be due to the limited number of observations. Figure 3.7 compares the typical polygonal structure with the longer wavelength observations.

Scaling wavelength λ by torus width W collapses the data to $\lambda/W \approx 1$ for the typical polygonal waves and $\lambda/W \approx 3$ for the long wavelength observations shown in blue in Figure 3.8. Thus, wavelength λ is essentially set by the torus width W as

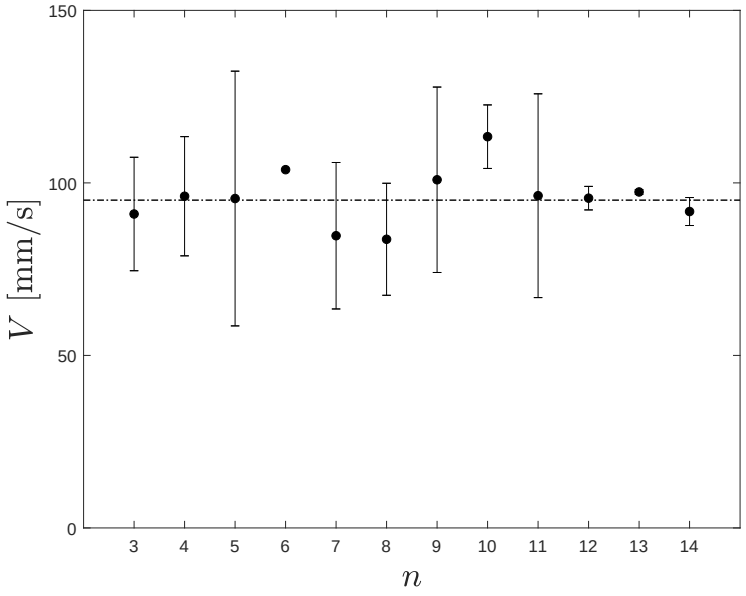

Figure 3.5: Rotational velocity V in mm/s plotted against mode number n. Error bars represent 95% confidence intervals.

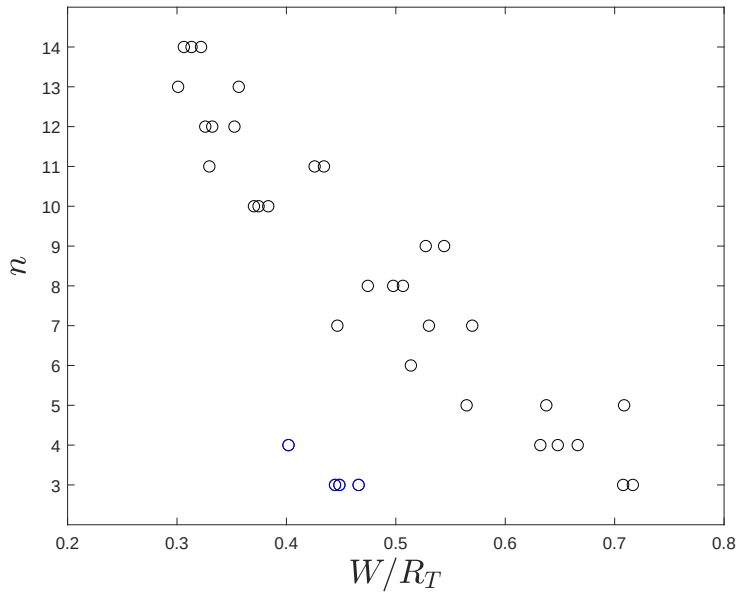

Figure 3.6: Mode number n vs aspect ratio W/R_T.

Figure 3.7: Comparison of the typical wavelength polygons (upper images) and long wavelength polygons (lower images) for $n = 3 - 4$.

this scaling shows that $\lambda \approx W$ for the typical wavelength observations and $\lambda \approx 3W$ for the long wavelength observations. For the long wavelength observations, we also observe pinching at the corners (cf. Figure 3.7) which we speculate to be caused by a Plateau-Rayliegh instability.

Several times we observed oscillations of the polygonal shape rather than the typical propagating polygonal wave. At their extrema, these oscillations are indistinguishable in shape from the propagating polygonal wave. Thus, we observe the same geometrical structure appearing during two characteristically different fluid motions. We observe oscillations of the polygonal shape for mode numbers $n = 3 - 5, 7$. We also observe star oscillations as reported in Chapter 2 appearing on the inner tori

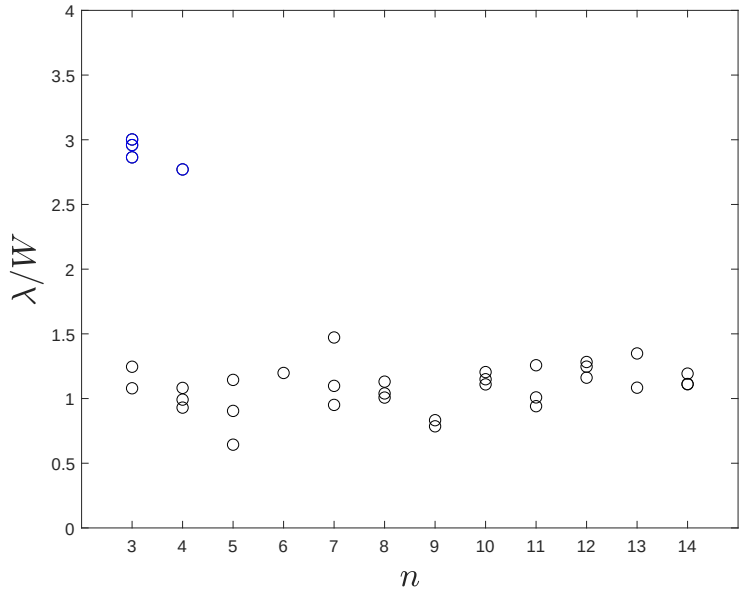

Figure 3.8: Scaled wavelength λ/W plotted against mode number n.

surface rather than the typical propagating polygonal wave. Star oscillations only appeared on the large torus plate and the inverted torus plate as will be discussed in Section 3.2.2.

3.2.2 Inverted torus plate

Figure 3.9 shows the equilibrium torodial configuration of water on the inverted torus plate. In this case the outer radius R_o is set by the volume of liquid. Again, torus height H is limited by $2l_c$ (Biance et al., 2003; Perrard et al., 2012; Quéré, 2013).

We report star oscillations appearing on the outer surface of liquid tori on the inverted torus plate. Using the inverted torus plate, we observe star oscillations for $n = 15 - 17$ shown in Figure 3.10. The oscillation frequency of these toroidal drops is found to be nearly constant $f \approx 12\,\mathrm{Hz}$, in agreement with our conclusion in Section

Figure 3.9: Static equilibrium toroidal shape on inverted torus plate.

2.5.1 for large water drops. We believe this conclusion holds true due to the similarity between drops in this toroidal configuration and large drops discussed in Chapter 2. The only difference being the exlusion of a liquid center in the toroidal configuration.

Figure 3.10: Liquid tori on inverted torus plate displaying $n = 15-17$ star oscillations.

The inverted torus plate essentially creates a large Leidenfrost drop excluding a liquid center. As noted in Section 1.4.2, the center of Leidenfrost drops become unstable for large R owing to the appearance of bubbles rising through the upper liquid surface. Here we remedy this instability by allowing vapor generated near the steep inner curvature to flow radially inward along the inner curvature. The majority of vapor is generated along the constant slope and escapes radially outward. This

allows the steady constant vapor flow to easily escape from underneath the large liquid tori without inducing the Rayleigh-Taylor instability. The outward flow of vapor is speculated to drive the star oscillations appearing along the outer liquid torus surface.

3.3 Discussion

We find that the static equilibrium shape is easiest to obtain at temperatures just above the Leidenfrost temperature T_L for both toroidal configurations. We believe the appearance of polygonal waves on the torus plate coincides with increased vapor flow underneath toroidal drops at higher temperatures. Increasing temperature well beyond T_L and adding flow tracers to the liquid tori, we have observed a poloidal flow in drops on the torus plate during the propagation of the polygonal wave in agreement with Perrard et al. (2012) who noted that the appearance of polygonal waves coincides with the observation of this poloidal flow. Due to the toroidal configuration of the liquid ($R_o > R_i$), this flow requires a difference in velocity at the inner and outer surfaces. The flow velocity along the outer surface at R_o must be higher than the velocity along the inner surface at R_i. We believe this difference in velocity is resolved by the reorganization of flow into the prefered polygonal shape. Further investigation into the cause of this poloidal flow may provide a better understanding of this complex phenomenon.

The poloidal flow is speculated to be caused by the underlying vapor flow u dragging the liquid surface above into poloidal motion where the liquid rises at R_i along the inner liquid surface causing a swift rolling motion of the liquid tori. This is reminiscinet of a similiar phenomenon of hydraulic jumps in which the rapid flow of a thin film beneath an overlying liquid causes vortices to develop in the overlying liquid. In experiments with highly viscous liquids, hydraulic jumps are observed with

a stable polygonal shape appearing along the inner liquid surface of the overlying liquid (Bush et al., 2006; Teymourtash and Mokhlesi, 2015). In these experiments, the polygonal wave is typically stationary with no rotation. We speculate that the rotation observed in our experiments is due to the vanishingly low friction presence in the vapor layer. However, we believe the physics governing both pattern formations on our liquid tori and hydraulic jumps is similiar.

Labousse and Bush (2015) presented a theorectical model based on the static equilibirum toriodial configuration and assumed vorticity to predict mode number n based on physical parameters of the liquid tori such as the Weber number We a relative measure of inertial effects to surface tension effects and an aspect ratio similiar to the one we defined earlier. The model agrees well for mode numbers $n = 5 - 9$ when compared to experiments by Perrard et al. (2012); however, we are unable to compare our results to this model due to limitations on measuring velocity in the liquid flow. Labousse and Bush (2015) also compares this theory with hydraulic jumps where vortex motion is thought to be greatly influencial in the formation of these polygonal structures. Labousse and Bush (2015) shows reasonable agreement between this model and hydraulic jumps.

We also believe, thermal instabilities such as Marangoni convection to play a role in the motion of liquid tori. Marangoni convection may cause a surface flow where the lower tori surface is at a higher temperature than the upper surface. This temperature difference induces a surface tension gradient which drives a surface flow from the lower surface to the upper surface. This surface flow may then induce a bulk motion poloidal flow contributing to this complex motion of liquid tori and the subsequent polygonal structures we observed here.

Using various substrate geometries, we were able to excite and study surface instabilities appearing on the free surface of toroidal drops in the Leidenfrost state.

We have shown how surface geometry greatly influences the fluid motion. We believe controlling surface geometry directly controls the underlying vapor flow u which is speculated in this thesis to give rise to the surface instabilities we have observed. Thus, surface geometry may be exploited to control the vapor flow and excite surface instabilities which can then be investigated experimentally and potentially quantified in an effort to understand the physics at play in this complex phenomenon.

Chapter 4

Conclusion

The Leidenfrost phenomenon has been expolited here to provide a free surface on which to investigate surface instabilities appearing on liquid drops. Experimental data was generated and presented in an effort to help elucidate the underlying physics governing the dynamic motion of Leidenfrost drops. In Chapter 2, we studied Leidenfrost star oscillations and have shown that the experimentally measured oscillation frequency f agrees reasonably well with the frequency predicted in the mathematical model developed in Section 2.4. We found that small drops $R < 4l_c$ oscillate with a frequency strongly dependent on radius. However large drops $R > 4l_c$ possess a single constant frequency independent of drop radius in agreement with Ma (2018). Mode doubling is observed in which two modes are excited simultaneously at different characteristic frequencies. We find the existence of a dominant $n = 2$ mode for drops of acetone, isopropanol, methanol, ethanol and liquid nitrogen over a large range of radii where typically higher modes n would be expected. Interpretations of these illuminating observations are given in an attempt to understand the physics governing Leidenfrost star oscillations.

In Chapter 3, we explored the effect of substrate geometry on the dynamics of

larger liquid volumes in the Leidenfrost state. We observed polygonal wave propagating along the inner liquid surface using our torus plate and star oscillations appearing along the outer liquid surface using our inverted torus plate. We presented our experimental data and provided a discussion on these results. We found the propagating wavelength λ to be approximately equal to the liquid tori width W and the propagation speed of this wave to be approximately constant $V = 95\text{mm/s}$. We believe the appearance of this wave is caused by a reorganization of the flow of liquid due to the inherent shape of the torus.

4.1 Future work

Improvements to the mathematical model are crucial in order to better understand the physics governing Leidenfrost star oscillations. Improvements to this model should account for viscous effects (Lundgren and Mansour, 1988) and frequency corrections due to the large amplitude of these oscillations (Tsamopoulos and Brown, 1983). Additionally, the pressure in the vapor layer should be accounted for in the model. A better mathematical model could be used to calculate liquid properties such as surface tension, density or viscosity as mentioned by Hervieu et al. (2001) and Haumesser et al. (2002).

In Section 2.3, we were able to target and excite subtle modes using a flat plate with a small depression which holds a drop in place under gravity. These drops were excited for a characteristic radius associated with the size of the depression and thus possessed characteristic frequency. We believe that substrates may be constructed in which a drop of particular radius may be excited with characteristic frequency based on the size of the depression. Therefore we could excite oscillations of characteristic radius and frequency using geometries targeted for each mode.

Using the inverted torus plate described in Section 3.2.2 we observe our typical star oscillations appearing along the outer periphery of the liquid torus. We observed water exhibiting $n = 15 - 17$ modes oscillating at the expected constant 12 Hz for water. It is well known that velocity and pressure fields are localized near the interface during capillary oscillations due to viscous dissipation (Lamb, 1932). Thus we conclude that the internal dynamics in the center of Leidenfrost drops are irrelevant during star oscillations as we have induced the same star oscillations on the periphery of a levitated liquid torus absent of internal liquid. We speculate this to be the reason for a stronger frequency dependence on radius for small Leidenfrost drops where viscous effects are not dissipated internally affecting the dynamics of oscillation. In contrast, viscous dissipation in large drops occurs internally away from the interface where surface oscillations occur. This may be verified experimentally using flow tracers to visualize the internal motion during Leidenfrost star oscillations. We believe investigating the influence of substrate geometry on Leidenfrost drops to be an abundant area of potential research that deserves further study.

Appendices

Appendix A Figures

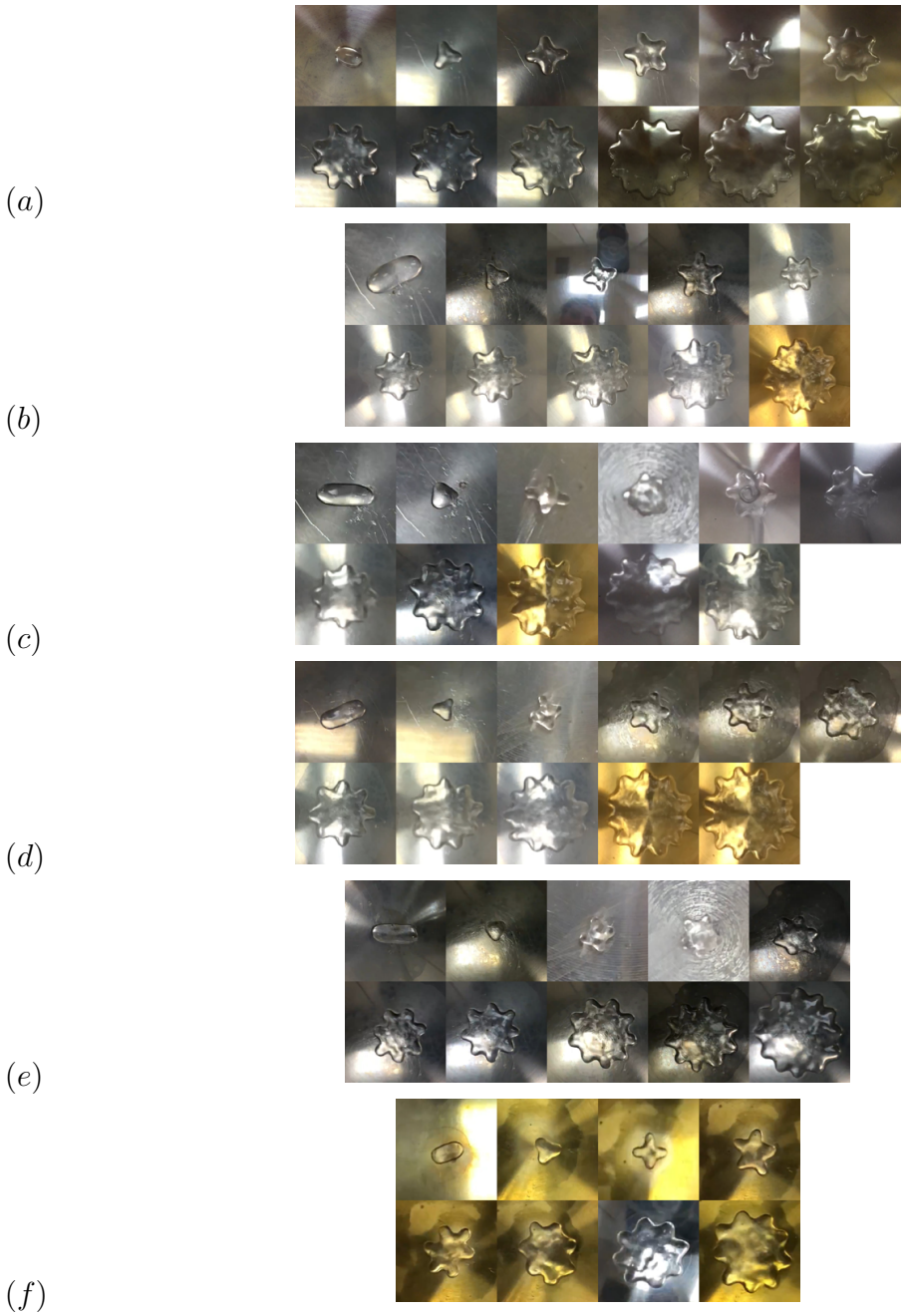

Figure A.1: Drops exhibiting all observed modes for each liquid (*a*) water, (*b*) acetone, (*c*) isopropanol, (*d*) methanol, (*e*) ethanol and (*f*) liquid nitrogen. Frames taken at an extrema during oscillation.

Bibliography

Adachi, K. and R. Takaki (1984). Vibration of a flattened drop. i. observation. *Journal of the Physical Society of Japan 53*(12), 4184–4191.

Aussillous, P. and D. Quéré (2001). Liquid marbles. *Nature 411*(6840), 924.

Aussillous, P. and D. Quéré (2006). Properties of liquid marbles. In *Proceedings of the Royal Society of London A: Mathematical, Physical and Engineering Sciences*, Volume 462, pp. 973–999. The Royal Society.

Avedisian, C. and J. Koplik (1987). Leidenfrost boiling of methanol droplets on hot porous/ceramic surfaces. *International journal of heat and mass transfer 30*(2), 379–393.

Baumeister, K., R. Hendricks, and G. Schoessow (1977). Thermally driven oscillations and wave motion of a liquid drop.

Baumeister, K. and F. Simon (1973). Leidenfrost temperature—its correlation for liquid metals, cryogens, hydrocarbons, and water. *Journal of Heat Transfer 95*(2), 166–173.

Baumeister, K. J., R. Henry, and F. Simon (1970). Role of the surface in the measurement of the Leidenfrost temperature.

Bergles, A. E., J. Collier, J. M. Delhaye, G. Hewitt, and F. Mayinger (1981). *Two-phase flow and heat transfer in the power and process industries*. Hemisphere New York.

Bernardin, J. and I. Mudawar (1999). The Leidenfrost point: experimental study and assessment of existing models. *Journal of Heat Transfer 121*(4), 894–903.

Biance, A.-L., C. Clanet, and D. Quéré (2003). Leidenfrost drops. *Physics of Fluids 15*(6), 1632–1637.

Bostwick, J. and P. Steen (2009). Capillary oscillations of a constrained liquid drop. *Physics of Fluids 21*(3), 032108.

Bostwick, J. and P. Steen (2013a). Coupled oscillations of deformable spherical-cap droplets. part 1. inviscid motions. *Journal of Fluid Mechanics 714*, 312–335.

Bostwick, J. and P. Steen (2013b). Coupled oscillations of deformable spherical-cap droplets. part 2. viscous motions. *Journal of Fluid Mechanics 714*, 336–360.

Bostwick, J. and P. Steen (2015). Stability of constrained capillary surfaces. *Annual Review of Fluid Mechanics 47*, 539–568.

Bouillant, A., T. Mouterde, P. Bourrianne, A. Lagarde, C. Clanet, and D. Quéré (2018). Leidenfrost wheels. *Nature Physics*, 1.

Boutigny, M. (1843). Sur les phénomenes que présentent les corps projetés sur des surfaces chaudes. In *Annales de Chimie et Physique*, Volume 3, pp. 350–370.

Bouwhuis, W., K. G. Winkels, I. R. Peters, P. Brunet, D. Van Der Meer, and J. H. Snoeijer (2013). Oscillating and star-shaped drops levitated by an airflow. *Physical Review E 88*(2), 023017.

Brunet, P. (2018). The crackling sound of Leidenfrost stars. *Journal of Fluid Mechanics 850*, 1–4.

Brunet, P. and J. H. Snoeijer (2011). Star-drops formed by periodic excitation and on an air cushion–a short review. *The European Physical Journal Special Topics 192*(1), 207–226.

Burton, J., A. Sharpe, R. Van Der Veen, A. Franco, and S. Nagel (2012). Geometry of the vapor layer under a Leidenfrost drop. *Physical review letters 109*(7), 074301.

Bush, J. W., J. M. Aristoff, and A. Hosoi (2006). An experimental investigation of the stability of the circular hydraulic jump. *Journal of Fluid Mechanics 558*, 33–52.

Caswell, T. A. (2014). Dynamics of the vapor layer below a Leidenfrost drop. *Physical Review E 90*(1), 013014.

Chang, C.-T., J. B. Bostwick, P. H. Steen, and S. Daniel (2013). Substrate constraint modifies the Rayleigh spectrum of vibrating sessile drops. *Physical Review E 88*(2), 023015.

Chang, H.-h. and E. A. Demekhin (2002). *Complex wave dynamics on thin films*, Volume 14. Elsevier.

Courty, S., G. Lagubeau, and T. Tixier (2006). Oscillating droplets by decomposition on the spherical harmonics basis. *Physical Review E 73*(4), 045301.

Fautrelle, Y., J. Etay, and S. Daugan (2005). Free-surface horizontal waves generated by low-frequency alternating magnetic fields. *Journal of Fluid Mechanics 527*, 285–301.

Gottfried, B., C. Lee, and K. Bell (1966). The Leidenfrost phenomenon: film boiling of liquid droplets on a flat plate. *International Journal of heat and mass transfer 9*(11), 1167–1188.

Haumesser, P.-H., J. Bancillon, M. Daniel, M. Perez, and J.-P. Garandet (2002). High-temperature contactless viscosity measurements by the gas–film levitation technique: Application to oxide and metallic glasses. *Review of scientific instruments 73*(9), 3275–3285.

Hervieu, E., N. Coutris, and C. Boichon (2001). Oscillations of a drop in aerodynamic levitation. *Nuclear engineering and design 204*(1-3), 167–175.

Holter, N. J. and W. R. Glasscock (1952). Vibrations of evaporating liquid drops. *The Journal of the Acoustical Society of America 24*(6), 682–686.

Jones, B. and J. Saylor (2009). Axis ratios of water drops levitated in a vertical wind tunnel. *Journal of Atmospheric and Oceanic Technology 26*(11), 2413–2419.

Labousse, M. and J. W. Bush (2015). Polygonal instabilities on interfacial vorticities. *The European Physical Journal E 38*(10), 113.

Lamb, H. (1932). *Hydrodynamics*.

Leidenfrost, J. G. (1756). *De aquae communis nonnullis qualitatibus tractatus*. Ovenius.

Lemmon, E., M. McLinden, D. Friend, P. Linstrom, and W. Mallard (2011). Nist chemistry webbook, nist standard reference database number 69. *National Institute of Standards and Technology, Gaithersburg*.

Lundgren, T. and N. Mansour (1988). Oscillations of drops in zero gravity with weak viscous effects. *Journal of Fluid Mechanics 194*, 479–510.

Ma, X. and J. C. Burton (2018). Self-organized oscillations of Leidenfrost drops. *Journal of Fluid Mechanics 846*, 263–291.

Ma, X., J.-J. Liétor-Santos, and J. C. Burton (2017). Star-shaped oscillations of Leidenfrost drops. *Physical Review Fluids 2*(3), 031602.

Miles, J. and D. Henderson (1990). Parametrically forced surface waves. *Annual Review of Fluid Mechanics 22*(1), 143–165.

Miles, J. W. (1957). On the generation of surface waves by shear flows. *Journal of Fluid Mechanics 3*(2), 185–204.

Nelson, A. R. and N. R. Gokhale (1972). Oscillation frequencies of freely suspended water drops. *Journal of Geophysical Research 77*(15), 2724–2727.

Okada, M. and M. Okada (2006). Observation of the shape of a water drop on an oscillating teflon plate. *Experiments in fluids 41*(5), 789–802.

Paquier, A., F. Moisy, and M. Rabaud (2015). Surface deformations and wave generation by wind blowing over a viscous liquid. *Physics of Fluids 27*(12), 122103.

Perez, M., Y. Brechet, L. Salvo, M. Papoular, and M. Suery (1999). Oscillation of liquid drops under gravity: Influence of shape on the resonance frequency. *EPL (Europhysics Letters) 47*(2), 189.

Perrard, S., Y. Couder, E. Fort, and L. Limat (2012). Leidenfrost levitated liquid tori. *EPL (Europhysics Letters) 100*(5), 54006.

Peterson, W. and M. Zaalouk (1971). Boiling-curve measurements from a controlled heat-transfer process. *Journal of Heat Transfer 93*(4), 408–412.

Pomeau, Y., M. Le Berre, F. Celestini, and T. Frisch (2012). The leidenfrost effect: From quasi-spherical droplets to puddles. *Comptes Rendus Mecanique 340*(11-12), 867–881.

Prosperetti, A. (2012). Linear oscillations of constrained drops, bubbles, and plane liquid surfaces. *Physics of fluids 24*(3), 032109.

Quéré, D. (2013). Leidenfrost dynamics. *Annual Review of Fluid Mechanics 45*, 197–215.

Rayleigh, L. (1879). On the capillary phenomena of jets. *Proc. R. Soc. London 29*(196-199), 71–97.

Shahriari, A., P. V. Acharya, and V. Bahadur (2018). Modeling the influence of Marangoni flows on the Leidenfrost state on solid and liquid substrates. In *ASME 2018 16th International Conference on Nanochannels, Microchannels, and Minichannels*, pp. V001T06A006–V001T06A006. American Society of Mechanical Engineers.

Shen, C., W. Xie, and B. Wei (2010). Parametrically excited sectorial oscillation of liquid drops floating in ultrasound. *Physical Review E 81*(4), 046305.

Snezhko, A., E. B. Jacob, and I. S. Aranson (2008). Pulsating–gliding transition in the dynamics of levitating liquid nitrogen droplets. *New Journal of Physics 10*(4), 043034.

Snoeijer, J. H., P. Brunet, and J. Eggers (2009). Maximum size of drops levitated by an air cushion. *Physical Review E 79*(3), 036307.

Soto, D. (2014). *Non-wetting drops: from impacts to self-propulsion*. Ph. D. thesis, Université Pierre et Marie Curie.

Strier, D., A. Duarte, H. Ferrari, and G. Mindlin (2000). Nitrogen stars: morphogenesis of a liquid drop. *Physica A: Statistical Mechanics and its Applications 283*(1-2), 261–266.

Takaki, R. and K. Adachi (1985). Vibration of a flattened drop. ii. normal mode analysis. *Journal of the Physical Society of Japan 54*(7), 2462–2469.

Teymourtash, A. R. and M. Mokhlesi (2015). Experimental investigation of stationary and rotational structures in non-circular hydraulic jumps. *Journal of Fluid Mechanics 762*, 344–360.

Tokugawa, N. and R. Takaki (1994). Mechanism of self-induced vibration of a liquid drop based on the surface tension fluctuation. *Journal of the Physical Society of Japan 63*(5), 1758–1768.

Trinh, E., R. Holt, and D. Thiessen (1996). The dynamics of ultrasonically levitated drops in an electric field. *Physics of Fluids 8*(1), 43–61.

Trinh, E. and T. Wang (1982). Large-amplitude free and driven drop-shape oscillations: experimental observations. *Journal of Fluid Mechanics 122*, 315–338.

Trinh, E., A. Zwern, and T. Wang (1982). An experimental study of small-amplitude drop oscillations in immiscible liquid systems. *Journal of Fluid Mechanics 115*, 453–474.

Tsamopoulos, J. A. and R. A. Brown (1983). Nonlinear oscillations of inviscid drops and bubbles. *Journal of Fluid Mechanics 127*, 519–537.

Vukasinovic, B., M. K. Smith, and A. Glezer (2007). Dynamics of a sessile drop in forced vibration. *Journal of Fluid Mechanics 587*, 395–423.

Wachters, L., H. Bonne, and H. Van Nouhuis (1966). The heat transfer from a hot horizontal plate to sessile water drops in the spherodial state. *Chemical Engineering Science 21*(10), 923–936.

Wang, T., A. Anilkumar, and C. Lee (1996). Oscillations of liquid drops: results from USML-1 experiments in space. *Journal of Fluid Mechanics 308*, 1–14.

Yoshiyasu, N., K. Matsuda, and R. Takaki (1996). Self-induced vibration of a water drop placed on an oscillating plate. *Journal of the Physical Society of Japan 65*(7), 2068–2071.

Zeisel, A., M. Stiassnie, and Y. Agnon (2008). Viscous effects on wave generation by strong winds. *Journal of Fluid Mechanics 597*, 343–369.

Zhang, X. (1995). Compressible cavity flow oscillation due to shear layer instabilities and pressure feedback. *AIAA journal 33*(8), 1404–1411.